In situ study of amorphous semiconductor crystallization by Dynamic Transmission Electron Microscopy

Shona McGowan

Department of Physics
McGill University
Montréal, Québec, Canada
August 2009

A thesis submitted to McGill University
in partial fulfilment of the requirements of the degree of
Master of Science

Abstract

Amorphous silicon is an important material of particular interest in the context of thin film transistors and display technologies. It also provides an ideal model system for the study of crystallization dynamics, and to this end we have investigated the crystallization of thin amorphous semiconducting films, including silicon and germanium, in the Dynamic Transmission Electron Microscope (DTEM) at Lawrence Livermore National Laboratory.

Crystallization is initiated in the DTEM by a laser pulse that deposits sufficient heat into the system to activate the transition. A variable time delay after this initiation pulse, the sample is probed by a short photoelectron pulse in the TEM, generating a diffraction pattern or image with nanosecond time resolution. Thus, using the DTEM we can gain access to the kinetics of crystallization and details of the nucleation mechanism *in situ* through time-resolved diffraction patterns and images of the specimen.

In the crystallized silicon film, three distinct phenomena were observed as the incident fluence on the sample was increased: for low fluences, the film underwent solid state crystallization, for surface melting, large, radially oriented crystals were observed and when the entire film was melted, the silicon dewetted from the substrate and coalesced into crystalline droplets on the surface. Modelling of heat conduction in the laser-heated film supports this interpretation. Preliminary experiments were also carried out in amorphous germanium.

Résumé

Le silicium amorphe est un matériau important en particulier, pour la fabrication de matériau polycristallin pour transistor couches minces. Il fournit également un système modèle idéal pour l'étude de la dynamique de cristallisation, et à cet effet, nous avons étudié la cristallisation des films couche mince en semiconducteurs amorphes, y compris le silicium et le germanium, dans le microscope Électronique en Transmission Dynamique (METD) à Lawrence Livermore National Laboratory.

La cristallisation est amorcée dans le METD par une Impulsion de laser qui dépose dans le système la chaleur suffisante pour activer la transition. Un délai variable après cette impulsion de déclenchement, l'échantillon est sondèe par une impulsion de photoélectron dans le MET, produisant soit diffraction ou une image avec la résolution temporelle de nanoseconde. Ainsi, utilisant le METD nous pouvons accéder à la cinétique de la cristallisation et les détails du mécanisme de nucléation emphin situ par les diagrammes diffraction et les images de l'échantillion avec résolution temporelle sur une échelle de nanoseconde.

Dans la pélicule cristallisée de silicium, on a observé trois phénomènes distincts à mesure que le fluence incident sur l'échantillon était augmenté : pour les fluences réduits, la pellicule a subi la cristallisation l'état solide, pour la fonte à la surface, des grands cristaux radialement orientés ont été produits et quand la pellicule entier a été fondu, le silicium fondu a été fusionnés dans les gouttelettes cristallines sur

la surface. La modélisation de la conduction de chaleur dans la pellicule chauffée par le laser soutient cette interprtation de l'évolution de la structure observée. Des exériences préliminaires ont été aussi effectuées en germanium amorphe.

Acknowledgements

Without the support and guidance of a great many people, this work could not have been completed. I would like to begin by thanking my supervisor, Dr. Bradley Siwick for his guidance, his patience, and his insight. Thanks are also due to the members of my research group: Vance Morrison, Robert Chatelain, Chris Godbout, and Andrew Bruhacs, for helping to make ours an enjoyable (if distracting) working environment. The DTEM team at LLNL was at once very welcoming and instrumental to my acquisition of the data presented here. I would specifically like to thank Thomas LaGrange and Bryan Reed for their helpful descriptions of DTEM operation and insight on troublesome diffraction data; James Evans for his tireless operation of a sometimes temperamental DTEM; Mitra Tehari for her feedback on results; and Nigel Browning who arranged my visit to LLNL. I also collaborated with Federico Rosei and Liliya Nikolova.

Thanks to the staff at the microfab: Matthieu Nannini, Pierre Huet and especially Don Berry for their advice and technical support. Many thanks to Jon Buset, for sharing his superior LaTeX skills with me, a mere mortal.

And of course, countless thanks to Wayne Bonnet for acting as a sounding board for my theories, contributing many hours of editing and helping me with MATLAB questions at the drop of a hat.

My friends and family have provided me with an abundance of support, and to them, to those listed above, and to those inadvertently omitted, I am entirely grateful.

Table of Contents

Abstract . . . iii

Résumé . . . v

Acknowledgements . . . vii

List of Figures . . . xi

List of Abbreviations . . . xiv

1 Introduction . . . 1

- 1.1 Motivation . . . 1
- 1.2 Background . . . 2
  - 1.2.1 Electron Microscopy . . . 2
  - 1.2.2 Ultrafast Electron Microscopy . . . 9
  - 1.2.3 Semiconductor Crystallization . . . 18
- 1.3 Thesis Objectives & Organization . . . 23

2 Experimental Methods . . . 25

- 2.1 Design Specifications of DTEM . . . 25
  - 2.1.1 Procedure for a DTEM Experiment . . . 28
  - 2.1.2 Limitations of the Current State of the Art . . . 29
  - 2.1.3 Experimental Parameters . . . 32
- 2.2 Sample Preparation . . . 33
  - 2.2.1 TEM Grid Fabrication . . . 33
  - 2.2.2 Amorphous film deposition . . . 35

3 Semiconductor Crystallization . . . 38

- 3.1 DTEM Images for a-Si . . . 38
  - 3.1.1 Laser Fluence Dependence of the Final Film Morphology . . . 38

3.1.2 Time-resolved Imaging of Amorphous Silicon Crystallization 40
3.2 Conventional TEM Imaging and Diffraction 44
3.3 Heat Diffusion and Estimate of Film Temperature 47
3.3.1 Analytical Solution 47
3.3.2 Heat Diffusion Model Including Melting 49
3.4 Inconsistencies in Experimental Results 56
3.5 Germanium Crystallization 57
3.5.1 Time-Resolved Results on a-Ge on SiO_2 58
3.5.2 'Cell'-like Structures Observed in a-Ge on SiN 59

4 Conclusion 63

4.1 Summary of Results 63
4.2 Future Work 64
4.2.1 Silicon 64
4.2.2 Germanium 65
4.3 Outlook 66

A Heat Diffusion Modeling 67

A.1 heatflow.m 67
A.2 runmodel.m 73

References 75

List of Figures

Figure page

1–1 Possible electron interactions with thin sample 3

1–2 Cross-sectional view of a magnetic lens for TEM 5

1–3 On the left is a perfect lens with no aberrations. The lens on the right exhibits spherical aberrations. 6

1–4 Schematic ray path for a conventional transmission electron microscope. 7

1–5 Phenomena classified by spatial and temporal resolution. Reprinted with permission from [32]. Copyright 2006, American Institute of Physics. 10

1–6 Timeline of development of UEM technologies [1] [2] [3] [4] [5] [6] [7] [8]. 12

1–7 Schematic of a TEM modified for dynamic imaging. 14

2–1 Schematic of the DTEM at LLNL. Reprinted with permission from [32]. Copyright 2006, American Institute of Physics. 26

2–2 Schematic of the photoelectron gun. 27

2–3 Spatial resolution limit for DTEM. The image on the left was taken with continuous illumination, the centre image is an average of 50 30 ns pulses and the image on the right was produced by a single shot. Reprinted with permission from [32]. Copyright 2006, American Institute of Physics. 31

2–4 Schematic of the TEM sample grids fabricated for use in the DTEM. 34

2–5 Fabrication process for TEM grids with SiO_2 windows. 36

2–6 Diffraction pattern on amorphous silicon film deposited by electron beam evaporation. 37

3–1 $t = \infty$ images for increasing fluence. All images were obtained from the same sample. The scale bar is $3\,\mu$m for all images. 39

3–2 Time series for $130\,$mJcm^{-2} laser pulse. (1a,2a) before exposure, $t = 0$ (1b) $t = 100\,$ns after the pump pulse, (2b) $t = 200\,$ns (1c,2c) $t = \infty$. 41

3–3 Time series for $140\,$mJcm^{-2} laser pulse. (1a,2a) before exposure, $t = 0$ (1b) $t = 100\,$ns after the pump pulse, (2b) $t = 300\,$ns (1c,2c) $t = \infty$ 42

3–4 Time series for $155\,$mJcm^{-2} laser pulse. (1,2a) before exposure, $t = 0$ (1b) $t = 100\,$ns after the pump pulse, 2(b) $t = 300\,$ns (1,2c) $t = \infty$. The arrows in panel (2b) indicate the moving boundary of what becomes the large crystalline region. 43

3–5 Time series for $180\,$mJcm^{-2} laser pulse. (1,2a) before exposure, $t = 0$ (1b) $t = 100\,$ns after the pump pulse, 2(b) $t = 300\,$ns (1,2c) $t = \infty$. 44

3–6 (a)TEM images, (b) diffraction patterns and (c) plot of intensity (arbitrary units) versus s for the three regions of interest. 46

3–7 Film temperature as a function of depth for an incident fluence of $180\,$mJ cm^{-2}. 48

3–8 Results of the heat conduction modeling for an incident fluence of $180\,$mJ cm^{-2}. 53

3–9 At boundary a sufficient energy is absorbed to melt the entire film. Between boundaries a and b, the film is only partially melted and outside boundary b, the film does not absorb enough energy to melt. 54

3–10 Heat diffusion modelling showing the temperature profile as a function of time at various depths in the silicon film. The temperature is plotted for the experimentally determined fluences (a) at the dewetting boundary ($330 \pm 20\,$mJ cm^{-2}) and (b) is at the surface melting boundary ($240 \pm 20\,$mJ cm^{-2}). 55

3–11 Time series for $135\,$mJ cm^{-2} laser pulse. (a) before exposure, $t = 0$ (b) $t = 100\,$ns after the pump pulse, (c) $t = \infty$. There is a small crystallized area at the centre of the pulse, but the remainder of the silicon film has delaminated from the substrate. 57

3–12 Time series for $115\,\mathrm{mJ\,cm^{-2}}$ laser pulse. (a) before exposure, $t = 0$ (1b) $t = 20\,\mathrm{ns}$ after the pump pulse, (2b) $t = 70\,\mathrm{ns}$, (3b) $t = 100\,\mathrm{ns}$, (c) $t = \infty$. The pump laser was not well aligned in the first set of images, so only the edge of the melted area is visible. The scale bar in each frame is $3\,\mu\mathrm{m}$. 60

3–13 Anomalous disk structures resulting from a single pump pulse in the DTEM. (a) pulsed image taken at $t = \infty$ in the DTEM (b - d) TEM images taken *ex situ* at various magnifications. The darkened area in (b) is due to the objective aperture in the microscope. . . . 61

List of Abbreviations

a-Ge	Amorphous germanium
a-Si	Amorphous silicon
DTEM	Dynamic Transmission Electron Microscopy
EC	Explosive crystallization
EELS	Electron Energy Loss Spectroscopy
FWHM	Full Width at Half Max
l-Si	Liquid Silicon
LLNL	Lawrence Livermore National Laboratory
LPCVD	Low Pressure Chemical Vapour Deposition
p-Ge	Polycrystalline germanium
p-Si	Polycrystalline silicon
RF	Radio Frequency
RIE	Reactive Ion Etching
SLG	Super Lateral Growth
TEM	Transmission Electron Microscopy
TFT	Thin Film Transistor
TMAH	Tetramethylammonium hydroxide

UED	Ultrafast Electron Diffraction
UEM	Ultrafast Electron Microscopy

CHAPTER 1

Introduction

1.1 Motivation

SINCE THE INVENTION OF THE TRANSISTOR, the ability to control crystal properties in semiconductors has been critical to the advancement of countless technologies. Much of our current understanding of the crystallization process is limited to using *in situ* techniques during processing, which do not directly access the spatial information on the microstructure of the sample in combination with *ex situ* imaging to examine the resulting grain size, orientation and defect concentration. As a result, attempts to achieve a structure with desirable properties have largely relied on trial and error, experimenting with different conditions for crystal growth, which is difficult since no information is available on the transient structures occurring as part of the growth process.

A knowledge of the intermediate structures leading to these properties would be invaluable in designing semiconducting structures to suit the needs of a variety of applications. These processes occur on a very short time scale, on the order of nanoseconds, which is difficult to access using conventional techniques. Furthermore, nanometer-scale or better spatial resolution is required to image the intermediate states. This union of high spatial and temporal resolution imaging represents an opportunity to extend our understanding not only in the dynamics of crystallization, but also many chemical and biological processes [9].

Recently, techniques have been developed which allow *in situ* study of phase transitions with nanometer spatial resolution and nanosecond time resolution. Dynamic Transmission Electron Microscopy (DTEM) marries two important technologies which have evolved in parallel to make such imaging possible: pulsed lasers and electron microscopy. In this pump-probe technique, crystallization is initiated by a laser pulse that deposits sufficient heat into the system to activate the transition, followed by a short photoelectron probe pulse after a variable time delay. This electron pulse is used t o obtain an image of the specimen.

A good understanding of the dynamics of crystal growth should lead to better control over the electrical, thermal and optical properties of the end product, in addition to answering several other outstanding scientific questions regarding crystal nucleation and grain growth.

1.2 Background

1.2.1 Electron Microscopy

The smallest features that can be observed using conventional optical microscopy is on the order of a micrometer. There are however, many structures of interest which exist on a smaller length scale, such as the morphology of cellular sub-structures, grain structure in materials or even individual atoms. In order to reach the nanometer or sub-nanometer scale resolution necessary to observe the structure of materials at a near-atomic level, a probe with a much shorter wavelength is needed. The obvious choices are X-rays, with wavelengths on the order of 100 pm, or electrons. A 200 keV electron has a wavelength of 2.5 pm.

Unlike X-rays, electrons are charged particles and interact with matter through the Coulomb force. X-rays interact only with the spatial distribution of the valence electrons, while incident electrons are influenced by the positively charged nuclei as well as the surrounding electrons. Thus electrons interact very strongly with matter through both elastic and inelastic scattering processes. Fig. 1–1 hows all the possible signals which are generated when an electron beam interacts with a sample interactions, including Auger, secondary and back-scattered electrons, X-ray radiation, visible light and heat. Techniques exist which take advantage of these processes to gain information about the sample, but will not be discussed herein.

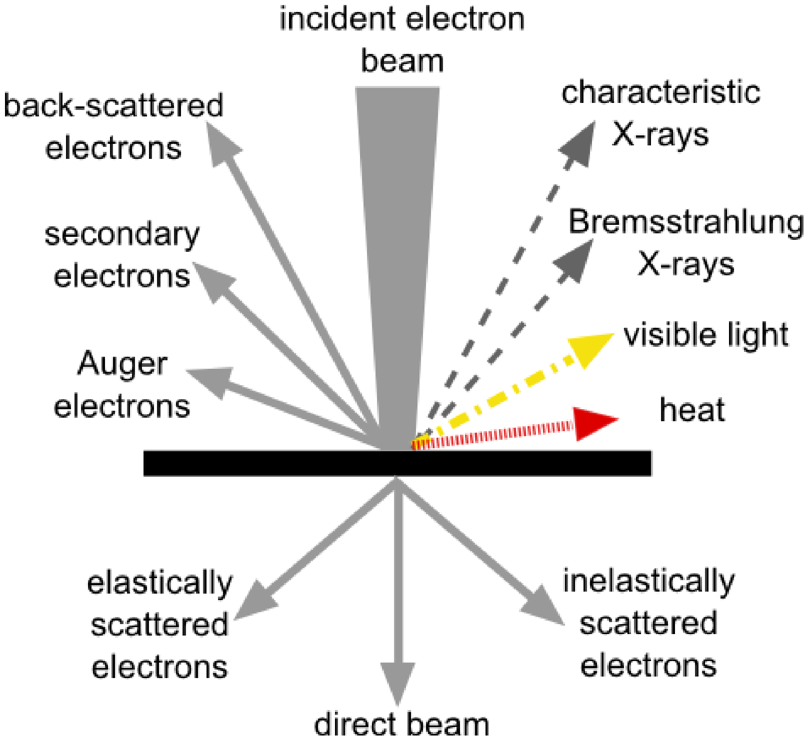

FIGURE 1–1: Possible electron interactions with thin sample

By collecting the scattered electrons, it is possible to gain structural information about the sample. For instance, the scattered electrons form a diffraction pattern which provides information about the crystal structure of the material. These diffraction patterns can be understood through Bragg's Law, which provides the condition for constructive interference:

$$n\lambda = 2dsin(\theta) \tag{1.1}$$

where n is an integer, λ is the wavelength of the electrons, 2θ angle between the incident and diffracted beams and d is the spacing between atomic planes for a simple cubic crystal, given by

$$d = \frac{a}{\sqrt{h^2 + k^2 + l^2}} \tag{1.2}$$

where a is the lattice constant for a cubic lattice and (hkl) are the Miller indices of the given plane. This is equally true for X-ray diffraction.

As these interactions are very strong, electron microscopy is limited to the study of surfaces or very thin samples, on the order of a few hundred nanometers thick for 200 keV electrons. This can be either an advantage or a disadvantage, depending on the application, as the properties of thin films can often be different than those in the bulk material, since surface effects play a much larger role.

Electron Optics

A major advantage of using electrons as opposed to X-rays is that electrons are fairly easily steered and focused transversely using electromagnetic fields. The effect of an electric field, $\mathbf{E}$, and a magnetic field, $\mathbf{B}$, on an electron is described by the Lorentz force equation:

$$\mathbf{F} = e(\mathbf{E} + \mathbf{v} \times \mathbf{B}) \tag{1.3}$$

where e is the charge of an electron and $\mathbf{v}$ is its velocity. This force can be used to shape and direct an electron beam in a manner analogous to the way standard optics are used for visible light.

Magnetic lenses, such as the one shown in Fig. 1–2, act much the same way as optical lenses; electromagnetic coils generate fields that act as a convex lens, focussing parallel rays at some constant focal length. Aberrations, such as astigmatism, and spherical and chromatic aberrations in electron optics make it very challenging to achieve atomic resolution, and thus the magnetic lens must be carefully designed to minimize these effects.

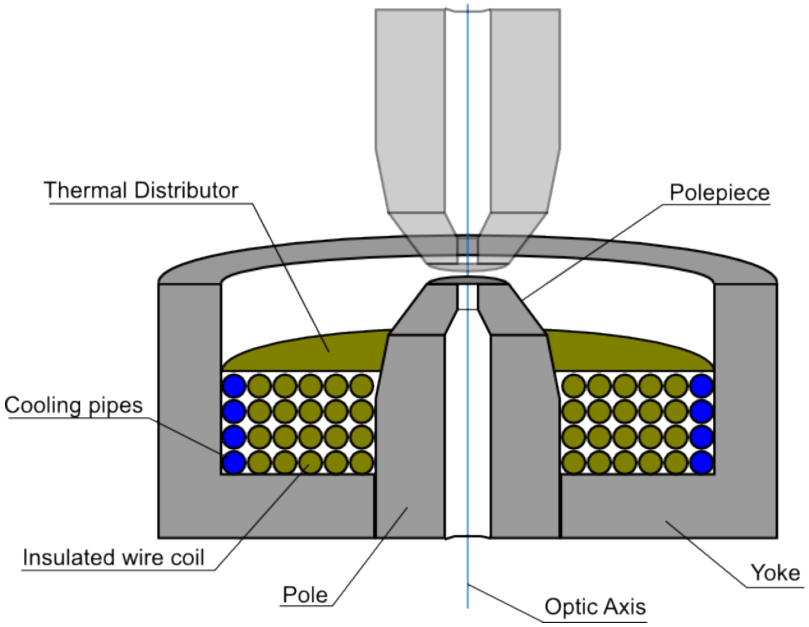

FIGURE 1–2: Cross-sectional view of a magnetic lens for TEM

Spherical aberrations are isotropic aberrations which occur in lenses with rotational symmetry. This type of aberration has the effect of reducing the focal length of the lens for electrons passing off the optical axis. This is shown schematically in Fig. 1–3. Spherical aberrations can be corrected by including higher order multipole lenses [10].

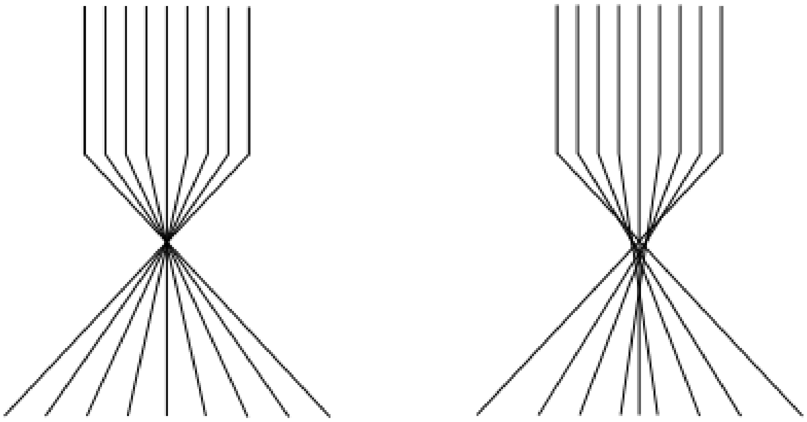

FIGURE 1–3: On the left is a perfect lens with no aberrations. The lens on the right exhibits spherical aberrations.

Chromatic aberrations are the result of an electron beam which is not monochromatic. For conventional electron imaging techniques, this energy spread may result from instability in the accelerating voltage, the statistical energy spread of the electrons as they are emitted from the source or energy losses in the specimen. Indeed an energy spread due to losses in the sample can be exploited to obtain information about the specimen using a technique known as Electron Energy Loss Spectroscopy (EELS).

Recently, there have been dramatic advances in spherical and chromatic aberration correction technologies. Implementing a hexapole corrector in combination with a monochromator has achieved resolution limits below 0.8 Å [10].

For an energy spread of δE, a point in the specimen will be imaged as a disc of diameter d_c' described by

$$d_c' = \frac{1}{2} C_c \frac{\Delta E}{E} \frac{1 + E/E_0}{1 + E/2E_0} \alpha_o M \tag{1.4}$$

where α_o is the aperture size, M is the magnification and C_c is the chromatic aberration coefficient, which is on the order of the focal length for weak lenses [11].

Transmission Electron Microscopy

Transmission Electron Microscopy (TEM) is a technique in which an electron beam is focused on a thin sample and the electrons which pass through the sample are used to generate an image or diffraction pattern. A schematic of the ray path in a typical TEM is shown in Fig. 1–4.

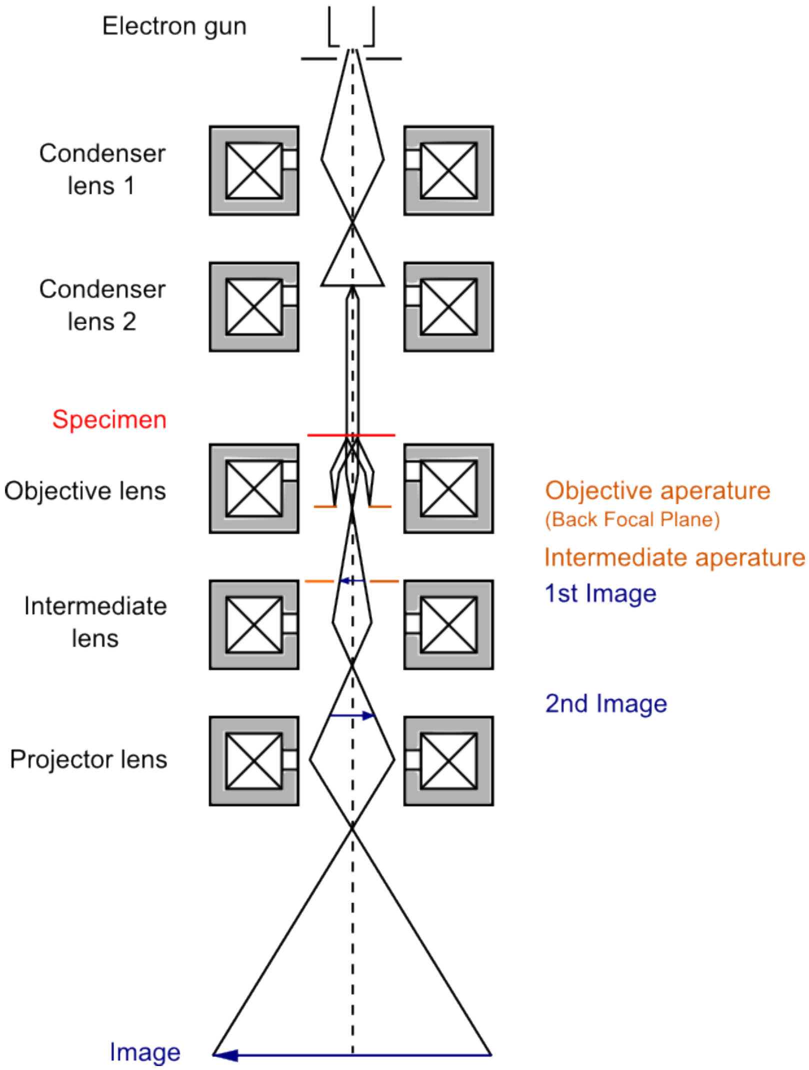

FIGURE 1–4: Schematic ray path for a conventional transmission electron microscope.

The electrons are emitted by a thermionic, Shottkey or field emission gun and accelerated down the optical column by an applied voltage. Typical acceleration voltages range from $100 - 300\,\mathrm{kV}$, but can reach up to $3\,\mathrm{MV}$ in high voltage TEMs. The electron beam leaving the gun is shaped by a series of condenser lenses which allows the illuminated area at the sample to be varied. At the sample, the electrons are scattered through elastic and inelastic processes, as shown in Fig. 1–1. Post sample, the electron intensity distribution is imaged by the objective lenses and projected onto a fluorescent screen. Images can be recorded on film or by a CCD camera coupled to a fluorescent screen by a fiber-optic plate.

Three standard modes of operation exist for a conventional TEM: bright field, diffraction and dark field mode. In bright field mode, the uninteracting electrons, those that pass through the sample without being scattered or absorbed, form the image. Thus, thicker regions of the sample appear darker and regions with no sample in the beam will appear bright. In addition, areas which diffract the beam, such as crystals oriented to satisfy a Bragg condition, will appear dark as the diffracted beam is blocked by the objective aperture in this mode of operation. The ray diagram in Fig. 1–4 shows a TEM operating in bright field mode.

When the TEM is operated in diffraction mode, the lens currents are adjusted such that the an image of the back focal plane (see Fig. 1–4) is placed on the screen instead of the imaging plane. The Bragg scattered electrons are dispersed to discrete points in the back focal plane according to Bragg's Law. The diffraction pattern will appear as a pattern of bright spots for a single crystal sample, as narrow rings in the case of a polycrystalline or as blurred rings for an amorphous sample. The diffraction mode provides complimentary information to bright field imaging since an image and diffraction pattern are given for the same sample region. This can help in the identification of the orientation of a single crystal or in establishing that a crystal phase is indeed present in the material when it may not be apparent in bright field mode.

Dark field contrast is obtained by imaging the Bragg diffracted electrons. The primary beam is tilted so that it is blocked by the objective aperture and the electrons which form a discrete diffraction spot are imaged in its place. As a result, the crystals which contribute to that diffraction spot will appear bright. Dark field mode is useful in distinguishing small crystallites which exist inside an amorphous matrix since these structures will appear bright while the surrounding amorphous material will appear dark.

1.2.2 Ultrafast Electron Microscopy

While TEM imaging and electron diffraction are very powerful tools for probing the structural properties of materials on length scales on the order of angstroms to nanometers, these techniques do not give an appreciation of the dynamic processes which lead to these structures or those that are occurring faster than the image acquisition time. A knowledge of the intermediate states provide valuable insight into the reaction or transformation pathways which lead to the final product. Fig. 1–5 provides an overview of a variety of interesting phenomena and the spatial and temporal resolutions required to properly investigate the processes.

In the 1980s, the development of ultrafast lasers capable of producing femtosecond pulses made it possible to perform spectroscopic experiments on the time scales of the fastest phase changes, chemical reactions and biological processes. However, this type of optical experiment typically measures spectroscopic quantities in the frequency or time domain, which do not directly provide information about the atomic positions. To gain direct access to the structural dynamics, diffraction or real-space

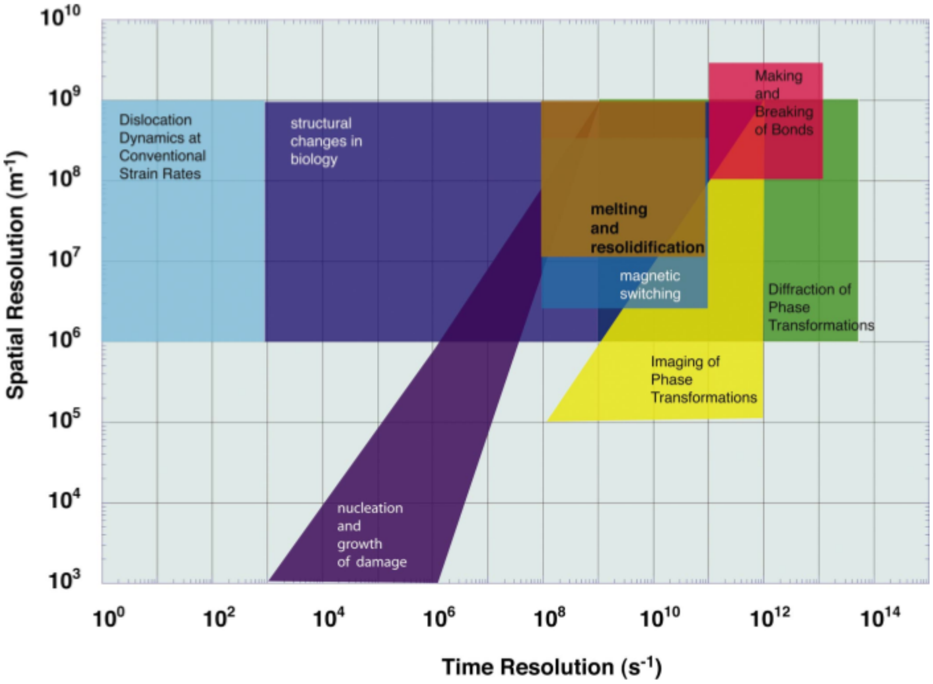

FIGURE 1–5: Phenomena classified by spatial and temporal resolution. Reprinted with permission from [32]. Copyright 2006, American Institute of Physics.

imaging at or near atomic resolution is needed. For the length scales of interest, this could be accomplished using either x-rays or electrons as the probe, however, there are several advantages to using electrons.

As discussed earlier, electron microscopy is a very well developed technique and dynamic imaging using electrons allows existing TEM material characterization techniques to be employed. Electrons are more strongly interacting than X-rays and thus do not penetrate as deeply. The scattering length of the electrons is more closely matched to the pumped volume of the sample, resulting in less contribution to the diffraction pattern from unpumped material. Electrons are also less damaging to specimens than X-rays since each useful interaction deposits less energy into the sample. This is of particular importance to the study of biological specimens, which have a very low damage threshold.

The first time-resolved electron microscopy experiments used beam blanking to pulse the electron beam. In the mid 1970s Bostanjoglo and Rasin obtained stroboscopic TEM images of ultrasonically pumped samples using this technique [1]. In the early 1980s, researchers began using photoemission to generate electron pulses. Many proceses have since been investigated using these photoelectron pulses including gas phase energy transfers [3], lattice heating [12], melting [7] [6], and multi-layer mixing [13]. Fig. 1–6 gives a brief history of the development of Ultrafast Microscopy technologies.

Ultrafast Electron Diffraction

Ultrafast Electron Diffraction (UED) is a powerful tool for probing the dynamics of phase changes, such as melting on very short time scales. Currently, time resolution on the order of a few hundred femtoseconds [14] [15] is achievable.

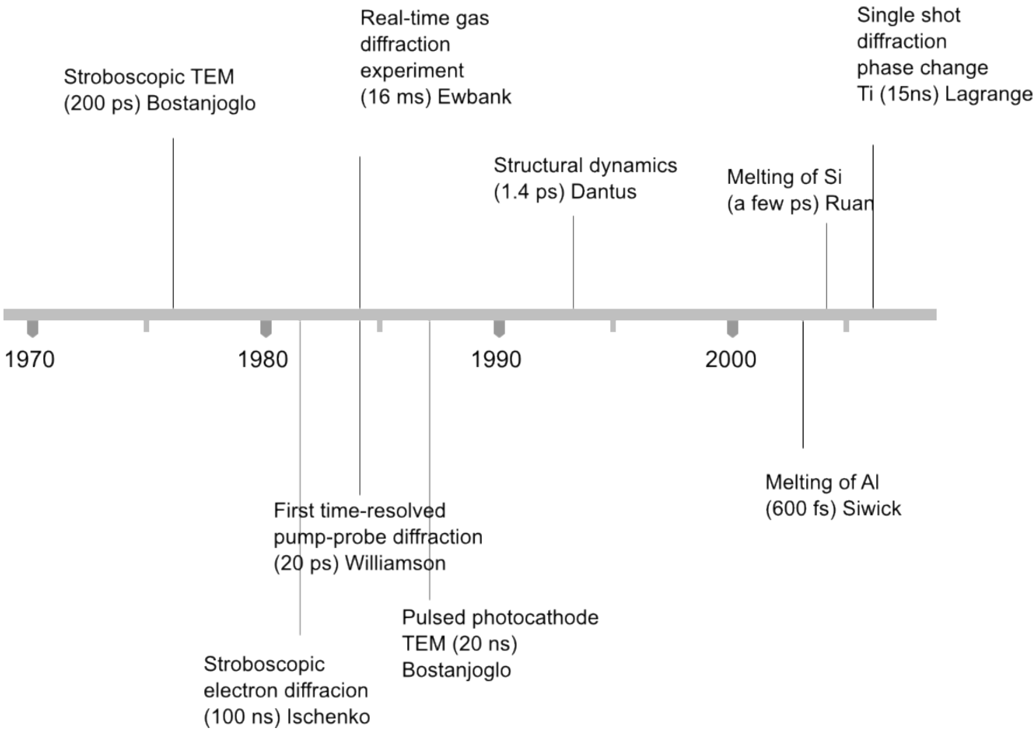

FIGURE 1–6: Timeline of development of UEM technologies [1] [2] [3] [4] [5] [6] [7] [8].

Conceptually, UED is very simple. A single laser pulse is divided into two parts: the pump pulse, which initiates the dynamics in the sample, and the probe pulse, which drives the electron gun. The time delay between the pump and probe pulses is accomplished by changing the path length of one pulse with respect to the other with a delay stage. Using this arrangement, it is possible to synchronize the pulses at the sample with a timing jitter of less than 100 fs [9].

The number of electrons per pulse is dictated by the cathode work function and the power density of the incident laser pulse. The time resolution of the system depends on the pulse length of the laser used to generate the photoelectrons and the distance from the photocathode to the sample. The latter is extremely important for femtosecond pulses, since electron - electron interactions result in the rapid expansion of the pulse in the time dimension. As a result of this pulse expansion, it is difficult to obtain ultrashort electron pulses with high current density. Typically, to generate a diffraction pattern with sufficient signal to noise, it is necessary to sum several time resolved patterns.

In order to obtain higher electron density, it is necessary to either implement some type of pulse compression or to use relativistic electrons. The Siwick group at McGill University together with collaborators at the Technische Universiteit Eindhoven have developed and are currently working to implement pulse compression using a radio frequency (RF) cavity . This approach makes use of the fact that the velocity distribution in the photoelectron pulse is linear, with the electrons at the leading edge being the fastest and those at the tail being the slowest. The oscillating field generated at the RF cavity retards the electrons at the front of the pulse while accelerating the electrons at the tail. Essentially, the velocity distribution of the electrons is reversed after the RF cavity. At some point down the line, the electron pulse will ballistically compress itself to a minimum time duration. If the sample is placed at this point, diffraction can be achieved with more electrons in a shorter pulse than ever before. With the RF compression scheme, it will be possible to generate sub-100 fs pulses with 0.1 pC per bunch [16].

Dynamic Transmission Electron Microscopy

Similar to UED, Dynamic Transmission Electron Microscopy is a pump probe experiment in which the dynamics of interest are initiated by a short laser pulse and probed at a variable time delay later by a photoemitted electron pulse. The apparatus consists of a conventional TEM which has been modified such that two laser pulses enter the column, one which excites the sample and the one which photoexcites the cathode to generate the electron pulse. Unlike in UED, the pump and cathode pulses are from two independent lasers, the relative timing of which are determined electronically. A schematic of this instrument is shown in Fig. 1–7.

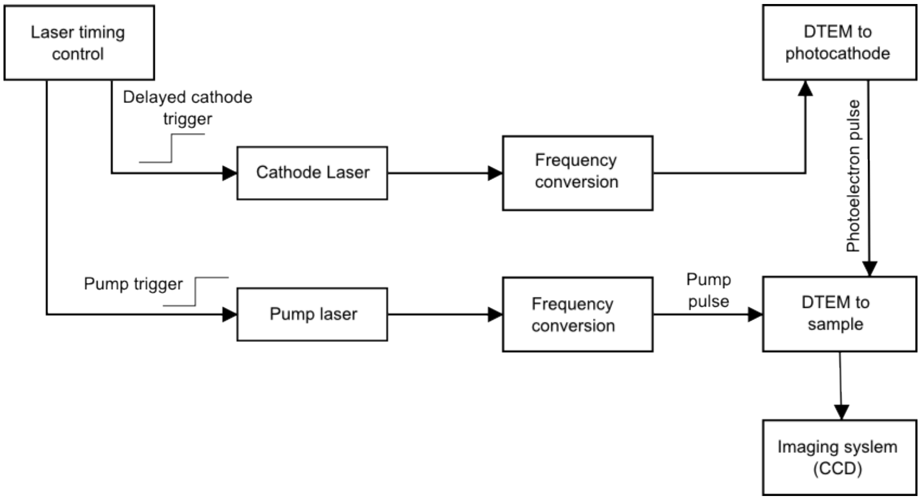

FIGURE 1–7: Schematic of a TEM modified for dynamic imaging.

In order to have sufficient signal to noise to produce an image with acceptable spatial resolution, on the order of 10^7 electrons are required. However, electron optics used in a conventional TEM are designed for an average of one electron in the column at a time. Significant chromatic aberrations result from the interactions between these electrons.

There are two ways to obtain sufficient signal for imaging: multiple images can be obtained and integrated using a stroboscopic technique, or a single short pulse can be generated with a sufficient number of electrons to produce an image. Both techniques have advantages and disadvantages.

The stroboscopic or multiple shot technique involves rapidly repeating an experiment and summing the results. Because the technique requires that the sample completely recover between shots, it is limited to studying fully reversible processes in which the sample reverts quickly to its original state.

The first DTEMs developed by Bostanjoglo in the 1970s were stroboscopic [1] and used beam blanking to obtain a pulsed electron beam. More recently, Zewail et al. has developed an instrument which uses an 80 MHz fs Ti:Sapphire oscillator to extract a single electron from a photocathode every 12.5 ns [17] [18]. Since one can repeat the experiment as many times as desired, it is possible to obtain very high resolution this way, comparable to conventional TEMs using this arrangement, but the range of experiments that can be studied is very limited.

In the single shot technique, one pulse of electrons is used to produce the image. This allows irreversible transitions, such as nucleation and grain growth, defect motion and transport, to be studied but currently limits the time resolution to nanoseconds. This resolution limit is a result of space charge effects, which cause an ultrashort electron pulse to expand, increasing the pulse length.Additionally, the spatial resolution available to this technique is significantly less than with the stroboscopic style experiments, also as a result of the space charge. Despite the difficulties that accompany the single shot technique, it is preferable for the majority of experiments since it is possible to study non-reversable phenomena.

In order to improve the time resolution of the single shot experiment, it may be necessary to accelerate electrons to relativistic velocities or use some form of pulse compression [9] such as those being implemented in current UED systems.

A microscope which uses the single shot technique with a 15 ns electron pulse has been developed at Lawrence Livermore National Laboratory (LLNL) . The technical details of this microscope will be discussed in Section 2.1. This is the microscope that was used to perform the studies on amorphous semiconductors, described in Chapter 3.

Space Charge

One of the major challenges in electron microscopy is mitigating space charge effects. This is especially true when a large number of electrons are emitted in short pulses such as in UED or DTEM.

In the absence of space charge the current density, J, is

$$J = (1-r)A_0T^2exp\left(\frac{-\phi}{kT}\right) \tag{1.5}$$

where r is the mean electron reflection coefficient of the cathode material, T is the cathode temperature and

$$A_0 = \frac{4\pi emk_B^2}{h^3} \tag{1.6}$$

where m is the mass of an electron, k is Boltzmann's constant, h is Planck's constant, and ϕ is the work function of the cathode.

In reality, the measured current density is much lower than the current predicted by Eq. 1.5. This is because most of the electrons emitted at the source are repelled by the neighbouring cloud of electrons. This is the space charge effect.

In the limit of large current densities, the Child-Langmuir effect describes a fundamental limit to the achievable current density emitted from a cathode as a function of the cathode-anode separation, d and the potential difference V_a:

$$I_a = JS = 2.33 \times 10^{-6} \frac{{V_a}^{3/2}}{d^2} \tag{1.7}$$

where I_a is the anode current per area. This limit is a result of the longitudinal space charge. Physically, as electrons are emitted from the cathode surface, a negatively charged cloud of free electrons is generated between the anode and cathode. So the effective acceleration voltage seen by the electrons at the cathode surface is the anode voltage *plus* the repulsive potential of the space charge. Eventually, the potential due to the space charge will be equal to the anode voltage, imposing a limit to the achievable current density. To obtain a high brightness source, such as required for high spatial resolution for single pulse TEM, the electron gun must have a high electric field at the source and a short accelerating length.

Longitudinal inhomogeneous space charge increases the energy spread of the electrons in the pulse according to the Boersch effect, leading to chromatic aberrations [19]. The mean energy is also shifted. These effects become more pronounced as the beam current is increased. Chromatic aberrations are the greatest challenge to obtaining high resolution in the DTEM because the spread in electron energy significantly degrades the contrast in images and causes blurring in diffraction patterns since the electron energy determines its wavelength.

Lateral space charge acts as a diverging lens to first order, defocusing the beam. Higher orders generate spherical aberrations. Lateral inhomogeneous space charge destroys high-resolution information stored in the lateral velocities. This information is used to obtain sub-nanometer resolution in high resolution TEM.

1.2.3 Semiconductor Crystallization

From a technological point of view, semiconductor crystallization is an important and well studied phenomenon due to implications in device fabrication, specifically in thin film transistors. Despite that there have been many related studies, the crystallization process in silicon is still not well understood. Most studies have relied on techniques such as time-resolved reflectivity measurements combined with post-experiment TEM imaging. While this technique can provide valuable information about the nucleation and growth rate of the crystals, which can suggest how the crystallization of the film proceeds, it is not ideal as it lacks direct spatial information as the imaging is performed ex-situ post crystallization. DTEM studies on these materials can provide complementary information which will serve to improve the understanding of the amorphous to polycrystalline transition in semiconducting materials.

Crystal Growth

The final structure of the crystallized film will be influenced by several factors, such as the absorbed energy, the type of substrate present, and the presence of impurities or nanocrystals in the amorphous film.

When an amorphous material is crystallized on a monocrystalline substrate, such as amorphous silicon (a-Si) deposited on a silicon wafer, the crystal structure of the newly crystallized film will match the structure of the substrate. This is known as epitaxial growth. The crystalline substrate acts as a seed crystal for the new growth.

When an amorphous film is crystallized on an amorphous substrate, such as a-Si on thermally grown SiO_2, the crystal nucleation and growth will be random, producing poly-silicon films. Experiments suggest that the thickness and quality of the oxide does not affect the nucleation and growth of the silicon. a-Si films deposited on either a thin native oxide or on a thicker layer of denser oxide exhibited the same crystallization kinetics [20]. Since the oxide does not seem to impact the kinetics, this suggests that the oxide/a-Si interface is not the dominant nucleation site. Further experiments performed in vacuum and in air suggest that the outer surface is also not the primary nucleation site. This leaves the interior of the film as the most likely site for nucleation. These studies involved furnace crystallization, where the samples are heated for an extended period of time at a constant temperature. The process which occurs in laser crystallization, which happens on a very short time scale, does not necessarily follow this behaviour.

Many groups report observing so-called 'explosive crystallization' (EC) [21] [22] [23]. This occurs when the maximum penetration depth of the laser induced melt is much less than the thickness of the amorphous film. At low energy densities, only the surface layer is melted by the laser. As this liquid solidifies to produce a polycrystalline layer, the latent heat released by the transition raises the temperature of the poly-crystalline silicon (p-Si) to above the melting point of a-Si, but remains lower than the melting point for crystalline silicon. As a result, the a-Si immediately below the initial melt layer begins to melt and subsequently crystallize, but with a smaller grain size than the initial melt region. Thus the final p-Si structure consists of a coarse grain crystalline layer near the surface with fine grained p-Si below. The total crystallized film is much deeper than the maximum penetration depth of the laser [24]. This structure was observed ex-situ by imaging cross-sectional slices of the crystallized silicon.

In 1993, Im et al. studied pulsed laser crystallization on 100 nm amorphous silicon films deposited by LPCVD on 100 nm SiO_2 substrates. The crystallization was initiated by a 30 ns XeCl excimer laser (308 nm). It was found that grain size increased gradually with increasing fluence until the average grain radius was approximately equal to the film thickness. Beyond this point, an extremely rapid increase in grain size was observed until a maximum size was reached, after which only small grains were produced once more.

These studies lead to the suggestion of the 'super lateral growth' (SLG) theory,which was used to explain the regime where large grain sizes were produced [25]. m suggests that at this point, nearly the entire film is melted, but there remain some small regions at the a-Si/ SiO_2 interface that are still solid. When the molten film subsequently crystallized, those unmelted grains act as the nucleation sites for the crystal growth.

Thin Film Transistors

A substantial force driving the study of the laser crystallization of amorphous silicon is the fabrication of thin film transistors . These are a type of field-effect transistor which are made by depositing a thin semiconducting film, a dielectric layer and metal contacts on a supporting substrate, typically glass. The primary application for such devices is in liquid crystal displays, hence the need for a transparent substrate material.

For fabricating TFTs, laser annealing is preferable to furnace annealing due to the faster processing time, and because it imparts minimal thermal damage to the glass substrate. Laser crystallization also has been shown to produce films with higher field effect mobilities (> $100\,\mathrm{cm}^2\mathrm{V}^{-1}\mathrm{s}^{-1}$) than films obtained by solid phase crystallization, despite the smaller average grain size [26]. However, excimer laser crystallization produces films of randomly oriented grains of non-uniform grain size, which is not ideal for TFT fabrication. This results in unreliable device characteristics [24]. An understanding of the crystallization process, particularly grain and defect formation, will help to determine the conditions required for optimal device fabrication.

Germanium

Although silicon is the most frequently studied semiconducting material, for its obvious technological impact, some studies on crystallization of amorphous germanium have also been performed. Germanium has very similar properties to silicon, which make it very complimentary to study in addition to silicon.

Early time-resolved TEM experiments were performed on amorphous germanium (a-Ge) samples by Bostanjoglo et al. [27] [28] using a frequency doubled Nd:YAG laser with 30 ns FWHM duration to irradiate 50 nm a-Ge samples evaporated onto rock salt. At laser fluence of $65-120\,\mu\mathrm{J/cm}^2$ the crystallization was found to be very fast; crytallization began $10-50$ ns after the arrival of the pump pulse, and was completed within $100-150$ ns. The final crystal structure was also fluence dependent. At low fluences (less than $60\,\mu$J/cm2), very fine grained central region surrounded by a ring of large, radially oriented crystals. At medium fluences ($65-120\,\mu\mathrm{J/cm}^2$) larger crystals were formed and the size decreased with increasing distance from the centre. At high fluences (above $130\,\mu\mathrm{J/cm}^2$) a large single crystal was formed at the centre, surrounded by smaller crystallites.

Thermodynamics of Crystallization: A simple model

The threshold energy for melting a thin film of thickness z can be estimated from the solution to the heat diffusion equation [29].

$$\frac{\partial T}{\partial t} = \frac{1}{\rho C_p} \frac{\partial}{\partial z} \left(k \frac{\partial T}{\partial z} \right) + \frac{\alpha}{\rho C_p} I(z,t) \tag{1.8}$$

where ρ is the density, C_p is the specific heat, k is the thermal conductivity, α is the optical absorption coefficient and $I(z)$ is the optical power density

$$I(z) = I_0(1-R)exp(-\alpha z) \tag{1.9}$$

where I_0 is the incident power density and R is the reflectivity. Assuming the material constants are not temperature dependent and that the thermal diffusion length, $\sqrt{Dt}$, is greater than the optical absorption depth, α^{-1}, the solution is:

$$T(z,t) = \frac{2I_0(1-R)\sqrt{Dt}}{k} ierfc \frac{z}{2L} \tag{1.10}$$

where

$$D = \frac{k}{\rho C_p}. \tag{1.11}$$

Taking

$$I_0 = \frac{E_0}{\tau} \tag{1.12}$$

where E_0 is the incident fluence on the sample and τ is the laser pulse duration, the surface temperature at the end of the pulse is

$$T(0,\tau) = \frac{2E_0(1-R)}{\sqrt{\pi}\rho C_p \sqrt{D\tau}}. \tag{1.13}$$

Thus, the threshold energy, E_T to raise the film surface to the melt temperature,T_m, from an initial temperature, T_0 is

$$E_T = \frac{(T_m - T_0)\sqrt{\pi}\rho C_p \sqrt{D\tau}}{2(1-R)}. \tag{1.14}$$

For a phase change (ie. liquid to solid, amorphous to crystalline) the latent heat of the transition, ΔH, also needs to be accounted for:

$$E \backsimeq E_T + \frac{\Delta H \Delta z}{\rho(1-R)}. \tag{1.15}$$

To take into account the temperature dependence of the thermal properties, it is necessary to solve the heat diffusion equation numerically. This will be discussed in chapter 3.

1.3 Thesis Objectives & Organization

The objective of this work is to study the laser initiated crystal nucleation and growth mechanism involved in the laser-driven amorphous to poly-crystalline transition in silicon and germanium *in situ* using Dynamic Transmission Electron Microscopy to obtain time-resolved real-space images. This process is of fundamental interest to the scientific community but these materials and laser processing methods also have significant technological relevance in display applications.

The organization of this thesis is as follows: In chapter 2 the experimental apparatus is described in detail, including the modifications made to the TEM at LLNL so that it could be operated in in pulsed mode. The advantages and limitations of the DTEM are discussed, and the details of the sample preparation are also described.

Chapter 3 and 4 present experimental results for amorphous silicon and germanium respectively. Time resolved images obtained using the DTEM at LLNL show the melting and crystallization of the semiconductors for different pulse energies. Analysis and discussion of the results are also included.

In chapter 5, the conclusions that have been drawn thus far are summarized and the direction for future work in this area is explored. The DTEM at LLNL is currently undergoing some remodeling and once these improvements have been implemented, additional experiments that were previously out of reach may now be possible.

CHAPTER 2

Experimental Methods

The time-resolved imaging was performed at Lawrence Livermore National Laboratory in Livermore, CA, using the Dynamic Transmission Electron Microscope developed there. The microscope uses a single shot technique to generate images with nanosecond and nanometer temporal and spatial resolution. Crystallization dynamics following laser exposure of amorphous silicon and amorphous germanium samples was studied. Thin films of each semiconductor were deposited by electron beam (e-beam) evaporation onto silicon dioxide windows. The procedure for preparing these samples is presented in this chapter, as well as the technical details of the DTEM and the experimental parameters used in this study.

2.1 Design Specifications of DTEM

The specifications of the microscope design are detailed by Armstrong [30] [31]. Briefly, a JEOL 2000FX 200 kV microscope was modified to introduce two lasers into the column: a pump laser, which excites the dynamics in the sample, and a cathode laser, which generates a photoelectron pulse. The time delay between these two pulses was controlled elecronically. A schematic of the modified microscope is given in Fig. 2–1

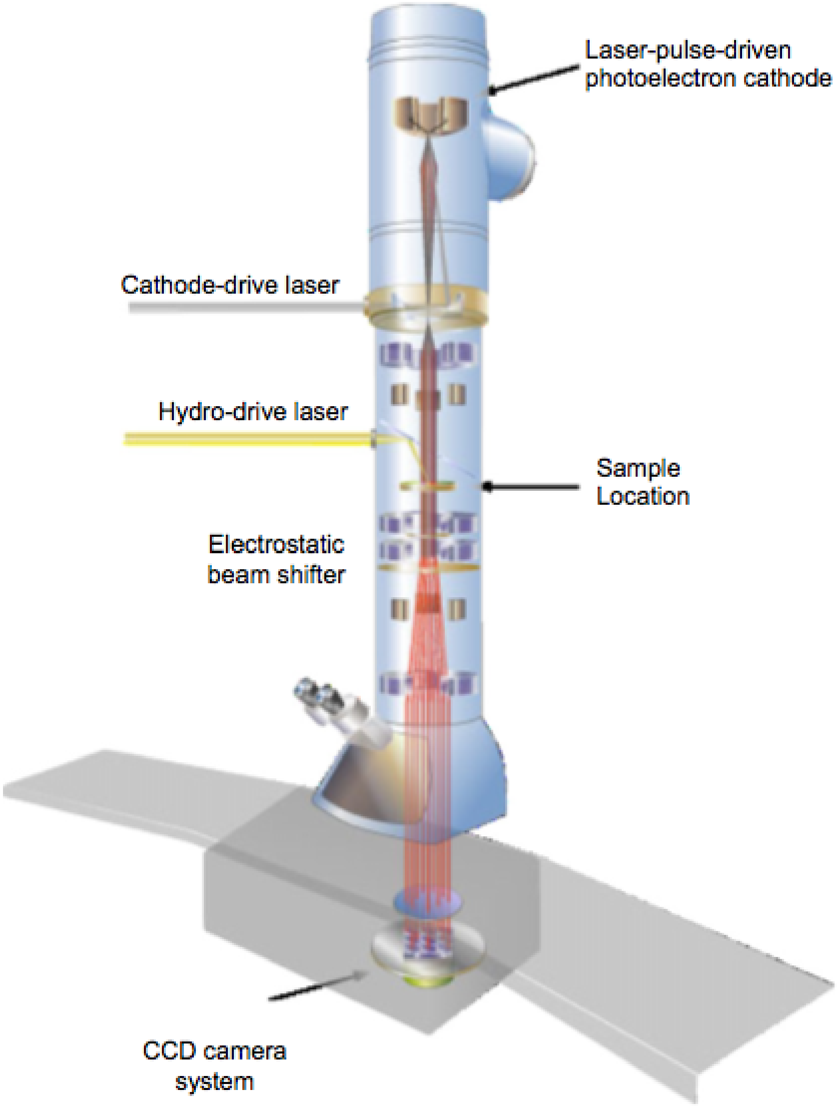

FIGURE 2–1: Schematic of the DTEM at LLNL. Reprinted with permission from [32]. Copyright 2006, American Institute of Physics.

The cathode laser is an Nd:YLF (Neodymium doped yttrium lithium fluoride, Nd : $LiYF_4$) laser with wavelength of 1053 nm and a pulse length of 70 ns. The pulse is frequency converted to the fifth harmonic (211 nm) before arriving at the cathode. The frequency converted pulse has a pulse length of 30 ns since the conversion process is non-linear. The laser pulse enters through a window in a small section added to the microscope column just below the electron gun. The pulse is directed upwards by an angled mirror to the photocathode, a 840 μm diameter tantalum disk. A hole in the centre of the mirror allows the photoelectron pulse to pass through to the condenser optics and the sample. The electron gun design is shown in Fig. 2–2.

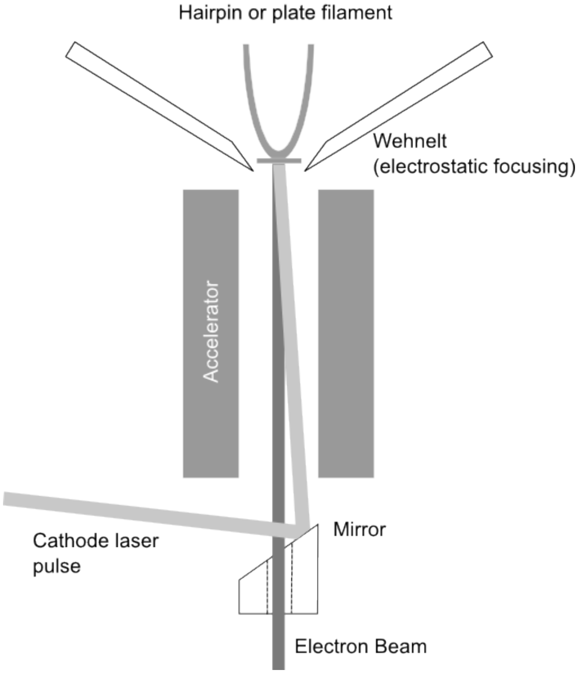

Figure 2–2: Schematic of the photoelectron gun.

The electron gun combines the photocathode disk with a hair pin filament, allowing the microscope to be operated in both thermionic and photoemission modes.

Thus, it is possible to image both in conventional, continuous beam mode as well as in the time-resolved, pulse beam mode.

The tantalum disk has photoemission quantum efficiency around 10^{-5} [32]. The energy incident on the cathode is $200\,\mu$J, which results in $3-4\times10^{7}$ electrons per pulse in the column. This is 10 to 100 times smaller than the theoretical electron yield, which is likely due to the inefficient collection of the electrons in the gun and condenser system. An additional condenser lens (C0 lens) was added to the column just below the gun to improve the collection efficiency.

The pump laser, which initiates the dynamics of interest in the sample, is a Nd:YAG laser (Neodymium-doped yttrium aluminum garnet, $\mathrm{Nd:Y_3Al_5O_{12}}$) with a wavelength of 1064 nm. This may also be frequency converted to better suit the absorption spectrum of the material under investigation. For the case of amorphous silicon, the pump pulse was frequency doubled to 532 nm. The energy of the pump beam incident on the sample is controlled using a waveplate polarizer combination. The pump laser enters through the x-ray port of the microscope and arrives at the sample at a 45° angle.

A time delay of 15 ns up to several microseconds [30] between the pump pulse and the photoelectron probe is accomplished through electronic triggering.

The image is captured by a single-electron sensitive CCD coupled to a phosphor screen. It is important the the detector is extremely sensitive since the number of electrons generating a single image is very low. The sensitivity of the current CCD is around 3-5 signal to noise for single electron detection.

2.1.1 Procedure for a DTEM Experiment

To perform an experiment, the pump laser must be aligned with the electron pulse on the sample. First, a coarse alignment of the electron beam is made with the microscope operated in 'continuous' or thermionic mode (electrons generated from the hair pin filament rather than the photocathode disk) to centre the beam on the screen. The microscope is switched to pulsed mode and the alignment is optimized.

The TEM sample holder can accommodate two samples at a time, and can switch from one to the other without breaking vacuum. Generally, one of the samples will be a sacrificial sample, usually a metal foil, which is used when aligning the pump laser with the electron probe. Using sufficient energy to ablate the material, the position of the pump beam on the sample is shifted using microcontrolled mirrors until the laser induced damage is centered in the image. Once the beams are well aligned, the sample of interest is inserted. It may be necessary to fine tune the laser alignment on this sample, especially if there is a substantial difference in the thicknesses of the two samples.

On a clean sample area, an image is taken using the pulsed electron probe without the pump laser. This shows the state of the sample before the dynamics are initiated ($t = 0$). The sample is then excited by the pump laser and a pulsed image is obtained after a short time delay. Finally, a last pulsed image is recorded several seconds or minutes later ($t = \infty$) which shows the final structure resulting from the laser heating. This process is then repeated for different time delays, choosing a clean sample area each time to build up a time series for the change.

2.1.2 Limitations of the Current State of the Art

Electron gun and optics design

A major challenge with the single shot technique is obtaining and maintaining the electron pulse. The electron gun must have high brightness and a cathode material with a high quantum efficiency in order to maximize number of electrons extracted. Brightness is defined as

$$B = \frac{Ne}{(\pi r^2)(\pi \alpha^2)\Delta t} \tag{2.1}$$

where N is the number of electrons per pulse, e is the electronic charge, r is the electron beam radius, α is the local convergence angle and Δt is the duration of the pulse [33]. It is equally important to collect the electrons as efficiently as possible while eliminating those that negatively impact the spatial resolution.

In an ideal imaging system, the gun brightness would be maintained throughout the column. However, this is not the case, and the brightness is significantly degraded due to the Boersch effect, aberrations and space charge effects by the time the electron pulse reaches the sample [33].

Working with a modified TEM imposes several limitations since the components are static; although the lens currents can be varied and apertures can be inserted or removed, the position of the lenses are fixed in the column and modifications to the column are major undertakings.

Coulomb interactions between the electrons traveling in the bunch will affect their trajectories, resulting in an irreversible loss of image information, called stochastic blurring. Stochastic blurring is intensified as the electron density and the pulse propagation time increase. High electron density is unavoidable at both the sample and at the back focal plane (where diffraction patterns are formed), so stochastic blurring cannot be completely eliminated. A balance must be found between the blurring effects resulting from high currents and the low signal to noise ratio at lower currents.

Spatial resolution

As a result of the strong interactions within the electron pulse, imaging with electron bunches makes high spatial resolution very difficult to achieve. Fig. 2–3 shows the limitation of the pulsed mode. The sample shown is alternating layers of gold and carbon with spacings of 20 and 30 nm. In the third image, which is produced from a single 30 ns electron pulse, it is becoming difficult to distinguish the 20 nm layer spacing. Currently, after some improvements to the imaging system, the resolution limit has been quoted as 10 nm. However, this limit applies for optimal conditions, and uses 'Z' contrast (related to the number of protons in a sample). The actual resolution limit for diffraction contrast is much worse, between to $20 - 50$ nm depending on the sample. The contrast is especially poor shortly after the laser pulse while the material is still hot.

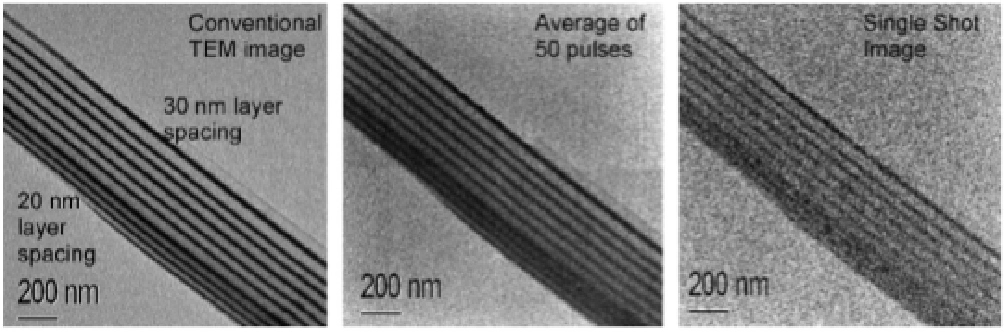

Figure 2–3: Spatial resolution limit for DTEM. The image on the left was taken with continuous illumination, the centre image is an average of 50 30 ns pulses and the image on the right was produced by a single shot. Reprinted with permission from [32]. Copyright 2006, American Institute of Physics.

Chromatic aberrations resulting from the initial energy spread of photoemitted electrons and exacerbated by electron-electron interactions as the electron bunch travels through the column are a major factor in the loss of spatial resolution for this microscope. Current chromatic aberration correction schemes are very expensive to implement, but would be highly beneficial for this application.

Repeatability of Experiments

Because the microscope is currently designed as a 'single shot' experiment, it is only possible to take one time resolved image per experiment. In order to build up a time series, multiple experiments must be performed at the same laser conditions on different sample areas. Thus the sample preparation is very important. Variations in the sample thickness, density, the presence of nanocrystals or other imperfections are difficult to avoid, but may have a large impact on the results. The preparation of the specimens will be discussed in the following section.

The DTEM is also not well suited for tracking the growth of a single crystal from nucleation to the final size since only one time resolved image is obtained per experiment at present. The nucleation of crystals can only be studied in an average sense, by repeating the experiment multiple times and compiling the results. Current plans to include a beam shifter will allow a train of electron pulses to be sent to the sample with various time delays. The beam shifter will rapidly deflect a train of electron pulses to different regions on the CCD such that multiple images can be obtained at different time delays within a single experiment, on a single CCD. Since there are fewer pixels on the CCD available for each image, the spatial resolution will suffer.

2.1.3 Experimental Parameters

The wavelength used to pump the samples in the DTEM was 532 nm. Originally we had used the third harmonic, 355 nm, but the experiments were not successful. There were several problems including difficulty producing sufficiently intense pulses at 355 nm to cause crystallization and trouble aligning the pump laser with the electron pulse. Using a UV pulse, it would have been easier to compare the results with the majority of studies, which use excimer lasers to induce surface melting. The absorption length in silicon is much longer at 532 nm (100 nm compared to 4 nm at 355 nm [26]).

Images were taken for time delays ranging from 20 to 400 ns using pulse energies up to 180 mJ cm^{-2}.

The laser spot size at the sample was approximately 100 μm $1/e^2$ diameter The energy required to produce a perceivable change in the structure varied from sample to sample. It is not yet known what the cause of this variability is, but it could be due to a number of factors, including variations in the density or thickness of the amorphous film, the presence of defects or impurities in the film or differences in the substrate from one sample to another. It is also possible that the differences are unrelated to the sample preparation and were the result of changes to the pump laser, such as a change in the spot size, over the course of the time of the experiments.

2.2 Sample Preparation

The samples used in this experiment were 130 nm of a-Si deposited by e-beam evaporation onto 50 nm SiO_2 windows grown by dry thermal oxidation. This thickness was chosen to ensure that the film was thicker than the absorption length at 532 nm.

2.2.1 TEM Grid Fabrication

Three millimeter diameter TEM grids with 9 100 μm$\times$100 μm windows, shown in Fig. 2–4, were produced in the microfabrication facilities at McGill University. SiO_2 membranes were used instead of the more durable and widely used SiN windows because of the oxide's long absorption length and low reflectivity at 532 nm. SiN absorbs strongly at this wavelength, and the window will frequently be damaged by the pump pulse, which prevents the study of the melt mediated crystallization.

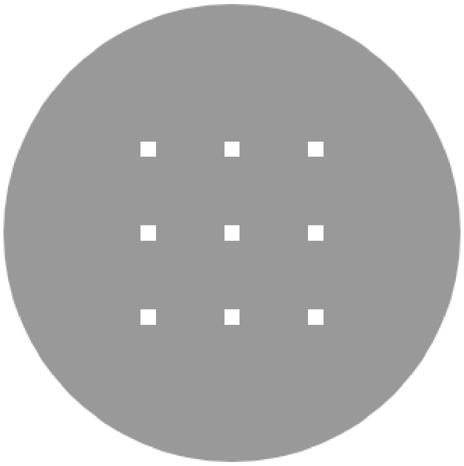

Figure 2–4: Schematic of the TEM sample grids fabricated for use in the DTEM.

The grids were fabricated from 250 μm thick, 100 mm diameter Si 100 wafers. Three hundred grids were patterned on a single wafer.

Approximately 60 nm of SiO_2 was grown on the clean Si wafer by dry thermal oxidation in a Tylan tube furnace at 1000 K. The thickness varied by about 5% over the full area of the wafer.

Following the oxide growth, a protective SiN layer was deposited by LPCVD to protect the oxide during the silicon etching stage. This layer was removed at the end of the process before the deposition of the amorphous film.

Next, the wafer was patterned and masked. One side of the wafer was spin coated with a 1.4 μm layer of positive photoresist (Shipley 1813), followed by a one minute soft bake at 115°C to remove excess solvent using the Site Coater Developer tool. The resist was then exposed to a 60 mJ cm^{-2} dose of UV light through the mask using the EVG620 Aligner. The resist was developed in the site coater and hardbaked at 90°C for 1.5 minutes.

Reactive ion etching (RIE), using the AMAT 5K RIE, was used to remove the SiN and SiO_2 exposed by the photoresist masked area. Both materials are etched by a the same combination of gases ($CF_4/CHF_3/Ar$). The etch rate is about 3500 Å/min. Following the RIE, the photoresist was removed using the PVA TePla Oxygen Asher for approximately 20 minutes. This left the samples with the silicon substrate masked by the SiN/ SiO_2 layer.

The patterned silicon was anisotropically etched with a 25% TMAH (tetramethylammonium hydroxide) solution by weight in water. The etch rate is $15-30\,\mu$m at 90° and the etch angle is 54.7° [34]. TMAH will also etch SiO_2 but at a much slower rate (less than 10 nm/hr) [34]. The oxide will essentially act as an etch stop for the silicon, and the silicon was allowed to over-etch for approximately one hour to ensure that it was complete.

Once the silicon is etched through, the grids were washed in distilled water to remove the excess etchant and particulate. The remaining SiN protective layer was etched away in a hot phosphoric acid bath at 90°C for about 5 minutes [35], followed by a rinse in distilled water once again.

This process yielded about 80% of the grids originally patterned on the silicon wafer. Because the oxide is very thin and fragile, about 20% of the windows broke during the etching stage.

2.2.2 Amorphous film deposition

There are many methods for depositing amorphous semiconducting films, including Low Pressure Chemical Vapour Depostion (LPCVD), Plasma Enhanced Chemical Vapour Depostion (PECVD), and various forms of Physical Vapour Deposition

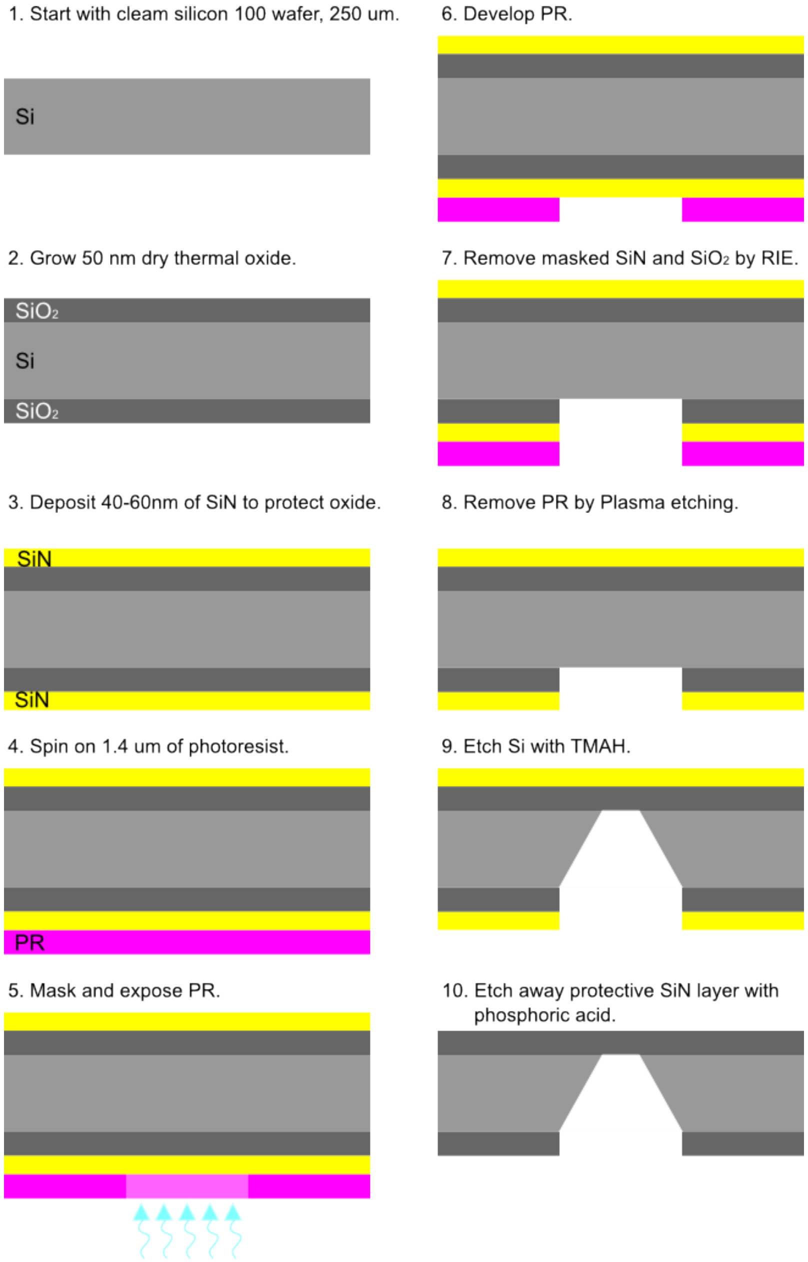

FIGURE 2–5: Fabrication process for TEM grids with SiO_2 windows.

(PVD). The chemical vapour deposition techniques generally use silane gas (SiH_4) as the source for the silicon. As a result, the thin films deposited in this manner contain some percentage of hydrogen, which can impact the crystallization of the film. To avoid hydrogenation, the films were deposited by e-beam evaporation.

Approximately 130 nm the material of interest, either a-Si or a-Ge, was deposited on the prepared TEM grids by e-beam evaporation at École Polytechnique. The films were evaporated at room temperature and at a pressure of 10^{-6} torr.

The samples were examined in a TEM to ensure that the semiconducting film was amorphous. Fig. 2–6 is a diffraction pattern taken on one of the silicon films. The diffuse rings clearly show that the film is amorphous and that no crystalline material is present.

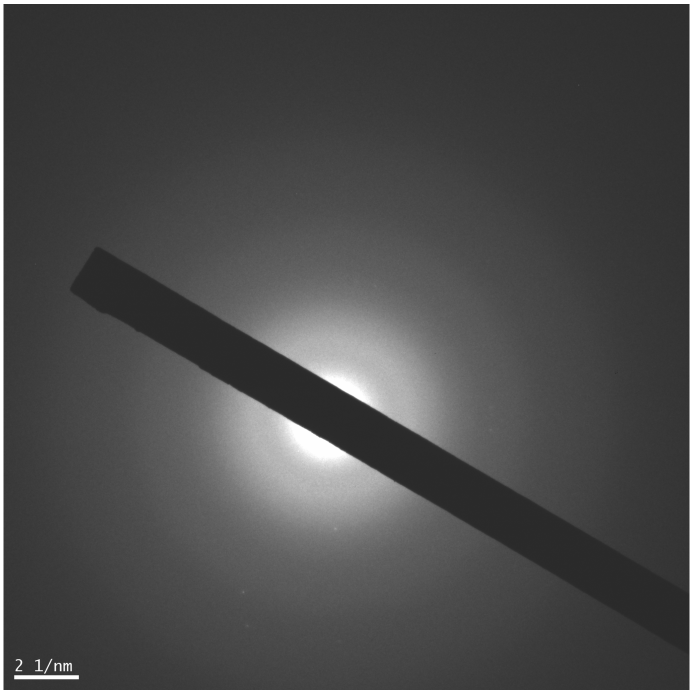

FIGURE 2–6: Diffraction pattern on amorphous silicon film deposited by electron beam evaporation.

CHAPTER 3

Semiconductor Crystallization

Amorphous silicon and amorphous germanium were studied in the DTEM at LLNL. On silicon, the fluence dependence of the final film morphology was investigated and time-resolved images were obtained for fluences ranging from 110 to $180\,\mathrm{mJ\,cm^{-2}}$. The results of these experiments, as well as modeling of the heat conduction in the thin silicon film is presented. Results of a preliminary study of a-Ge crystallization are also discussed.

3.1 DTEM Images for a-Si

3.1.1 Laser Fluence Dependence of the Final Film Morphology

The crystallization process of a-Si following nanosecond laser exposure was observed *in situ* for a range of laser energies in the DTEM at LLNL. Fig. 3–1 shows images of the final state ($t = \infty$) for the fluence range explored on one sample. Three distinct regions exist for high pulse energies: (1) at the centre of the laser pulse, where the film will have been hottest, the large dark balls are silicon which has coalesced on the mostly bare SiO_2 substrate (light contrast region) to form polycrystalline droplets, (2) the central melted region is surrounded by a ring of $10 - 15\,\mathrm{nm}$ long radially oriented crystals, and (3) at the edge of the large crystalline region, smaller crystals, a few hundred nanometers in diameter, are present. At lower energies, only the 2nd and 3rd regions are present, and the size of the large crystalline region decreases as the pulse energy decreases. Since the exciting laser pulse is gaussian, this corresponds to a smaller area absorbing enough energy to surpass the temperature threshold for this growth mode.

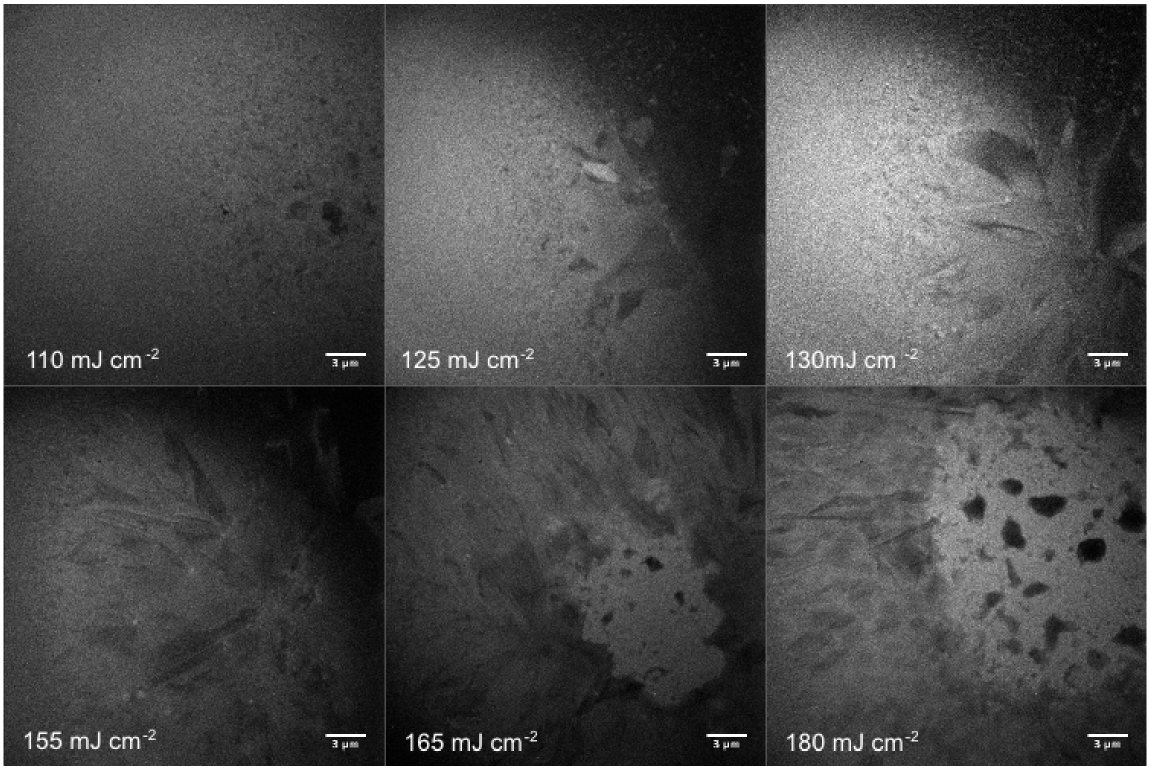

FIGURE 3–1: $t = \infty$ images for increasing fluence. All images were obtained from the same sample. The scale bar is $3\,\mu$m for all images.

At high fluences, the a-Si film has completely melted at the centre of the laser pulse. The liquid Si (l-Si) has dewetted from the substrate and balled up into droplets of varying size, ranging from tens of nanometers (which cannot be seen in the time resolved images, but are present in Fig. 3–6.1a) up to $5\,\mu$m. From images obtained from the same specimens exposed in the DTEM at LLNL, taken in the TEM at

McGill, it has been confirmed that these droplets are indeed crystalline or polycrystalline (see Fig. 3–6).

In the large ring of radially oriented crystal grains, it is probable that the melting temperature was reached, but that the film was not melted all the way to the substrate. In this case, the film would not dewet from the substrate as it has for higher energies since the silicon at the sample-substrate interface. remains solid.

The smaller crystallites at the edges most likely result from solid state crystallization of the film, which remained below the melt temperature. Crystals in this region ranged from 10 nm up to 200 nm.

To verify this interpretation of the morphologies observed, the heat diffusion in the a-Si thin film has been modeled. The results of the modeling are presented in Section 3.3.2.

3.1.2 Time-resolved Imaging of Amorphous Silicon Crystallization

3.1.2.a Average Laser Fluence = $130\,\mathrm{mJ\,cm^{-2}}$

In Fig. 3–2, a $130\,\mathrm{mJ\,cm^{-2}}$ pulse was used to heat the sample. At 100 ns after the laser pulse the crystal structure is not yet visible.There are, however, a number of randomly distributed light spots that have appeared, which remain unchanged between 100 ns and the final state image. In these regions the film has dewetted locally, exposing the substrate. Conventional TEM imaging performed post exposure at higher resolution shows that these areas closely resemble the melted regions at the pulse centre for higher pulse energies (Fig. 3–1).

At 200 ns, the crystallization of the film appears to be complete. There is minimal difference between Fig. 3–2.2b and Fig. 3–2.2c aside from the improved contrast in the final image, which indicates that the film has cooled. The small crystallites at the boundary of the large radially crysallized region are also visible in this image.

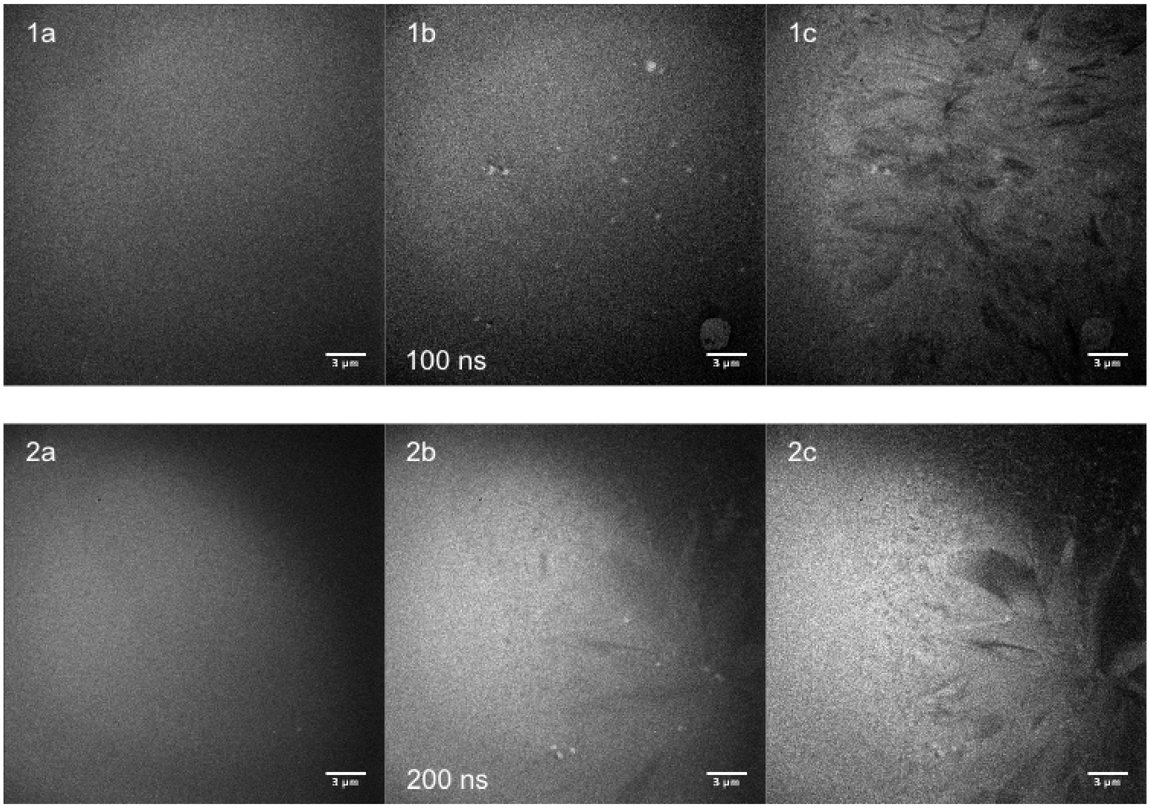

FIGURE 3–2: Time series for 130 mJcm^{-2} laser pulse. (1a,2a) before exposure, $t = 0$ (1b) $t = 100$ ns after the pump pulse, (2b) $t = 200$ ns (1c,2c) $t = \infty$.

3.1.2.b Average Laser Fluence = 140 mJ cm^{-2}

At 140 mJcm^{-2}, the final crystal structure is very similar to that obtained at the lower fluence, however, the time to reach this structure was longer. At 300 ns (Fig. 3–3.2b) the large crystal grains are visible, but still changing. In Fig. 3–3.2 the pump laser was not well centered with respect to the electron pulse, so only the periphery of the crystallized region was captured.

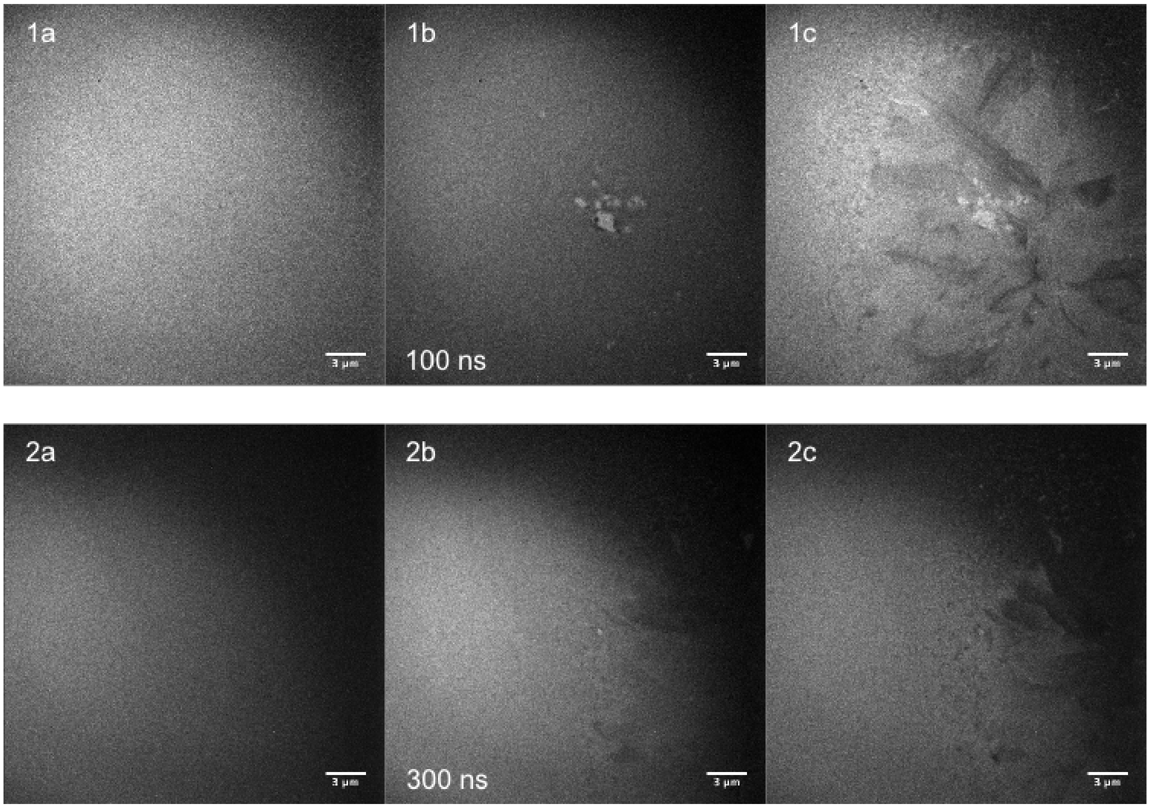

FIGURE 3–3: Time series for 140 mJcm^{-2} laser pulse. (1a,2a) before exposure, $t = 0$ (1b) $t = 100$ ns after the pump pulse, (2b) $t = 300$ ns (1c,2c) $t = \infty$

3.1.2.c Average Laser Fluence = 155 mJ cm^{-2}

For a 155 mJ cm^{-2} incident pulse, the final structure again consists of long radially oriented grains, but this region is larger in diameter than it was at the lower energies. At 300 ns, the film does not show much evidence of crystallization, unlike the two previous images. The different crystallization times for these three energies are likely due to the higher the input energy; the higher the film temperature post-exposure, the longer it will take to cool sufficiently to resolidify.

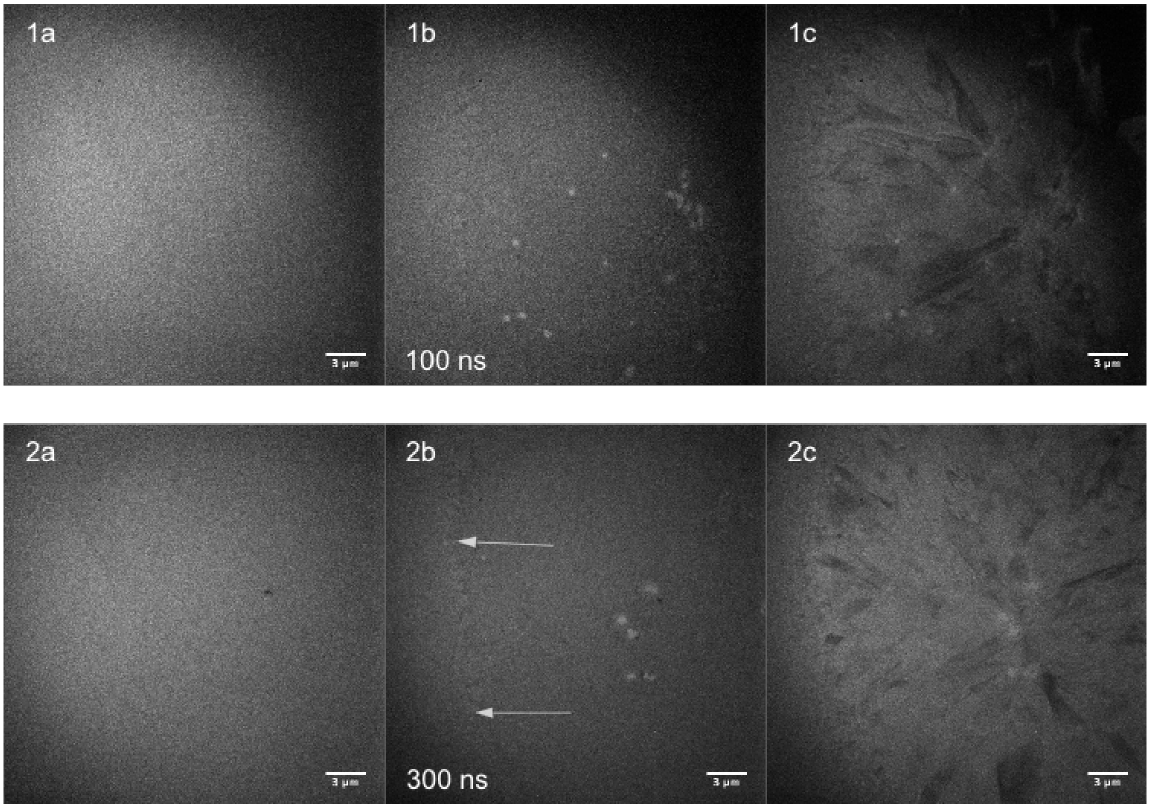

FIGURE 3–4: Time series for 155 mJcm^{-2} laser pulse. (1,2a) before exposure, $t = 0$ (1b) $t = 100$ ns after the pump pulse, 2(b) $t = 300$ ns (1,2c) $t = \infty$. The arrows in panel (2b) indicate the moving boundary of what becomes the large crystalline region.

In Fig. 3–4.2b, there is a distinct ridge visible (indicated by arrows). This ridge corresponds to the outer edge of the large grain region in the $t = \infty$ image. This is the outer boundary of the region which was hot enough to melt at least a surface layer, as evidenced by the dramatic change in the crystal size that occurs across this boundary: from large radially oriented crystals to small-grained p-Si.

3.1.2.d Average Laser Fluence = 180 mJ cm^{-2}

The pulse energy used to produce Fig. 3–5 was sufficient to produce complete melting at the centre of the film. The 180 mJ cm^{-2} laser pulse caused the a-Si to dewet (Fig. 3–5.1b) and coalesce (Fig. 3–5.2b) to form crystalline or polycrystalline droplets ranging from a few micrometers in size down to a few nanometers, which are too small to see in the DTEM images. Once again, the interface between solid and liquid silicon is visible at 300 ns.

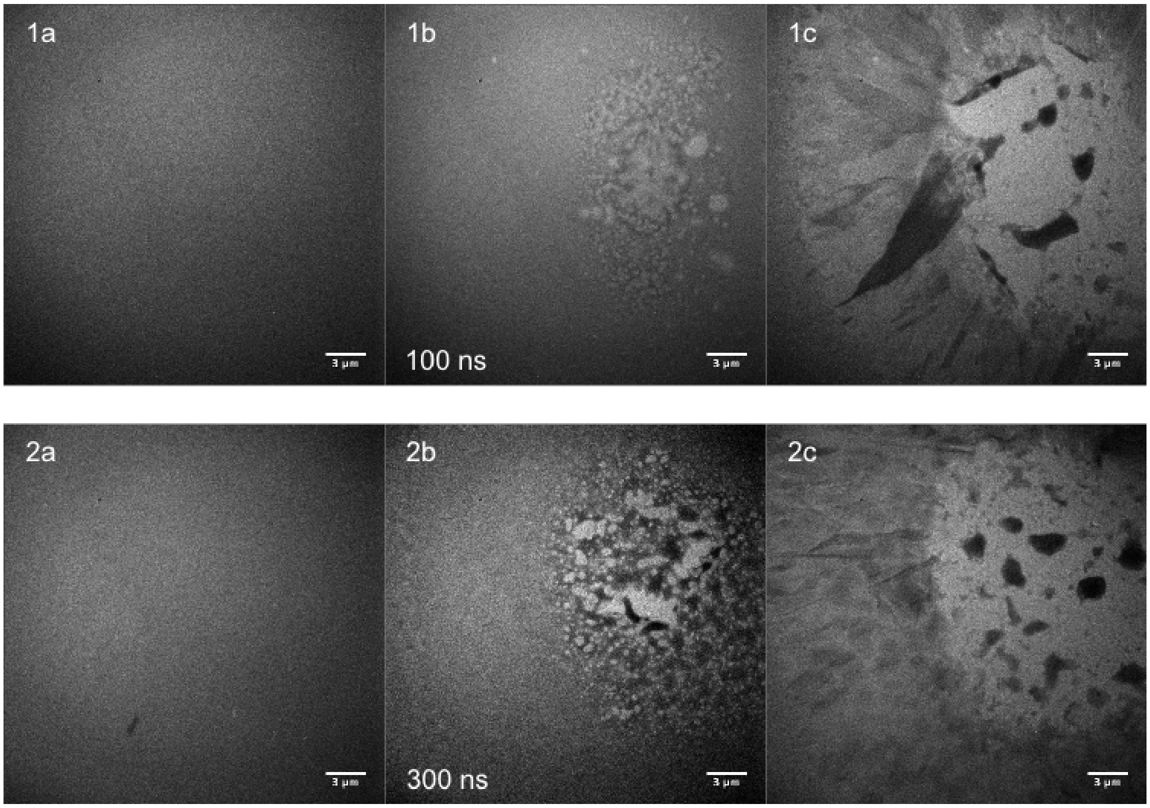

FIGURE 3–5: Time series for 180 mJcm^{-2} laser pulse. (1,2a) before exposure, $t = 0$ (1b) $t = 100$ ns after the pump pulse, 2(b) $t = 300$ ns (1,2c) $t = \infty$.

3.2 Conventional TEM Imaging and Diffraction

Conventional TEM imaging was performed at McGill on the samples exposed in the DTEM at LLNL. Unfortunately, the sample on which the images presented in this chapter were obtained was severely damaged in transit, limiting the extent of imaging possible. Only one partially broken window was available on the sample. Fig. 3–6 shows (a) bright field images and (b,c) diffraction patterns taken on that window.

Fig. 3–6.1a shows the centre region for a high pulse energy. The large crystallized droplets measure up to 5 μm in diameter, while the smaller crystals are on the order of 100 nm. The diffraction pattern for the dewetted area is dominated by the amorphous diffraction pattern from the amorphous SiO_2 substrate.

In the second region (Fig. 3–6.2a) the crystal grains were up to 15 μm long (in the radial direction) and approximately 2 μm wide. The diffraction pattern shows that there are several crystal orientations present in the selected area, which suggests that there is not a preferred crystal orientation.

Further still from the centre of the laser pulse, the film is polycrystalline with crystal grains ranging from 20 to 200 nm (Fig. 3–6.3a). The powder-like diffraction pattern in Fig. 3–6.3b supports the idea that the crystals are small and randomly oriented.

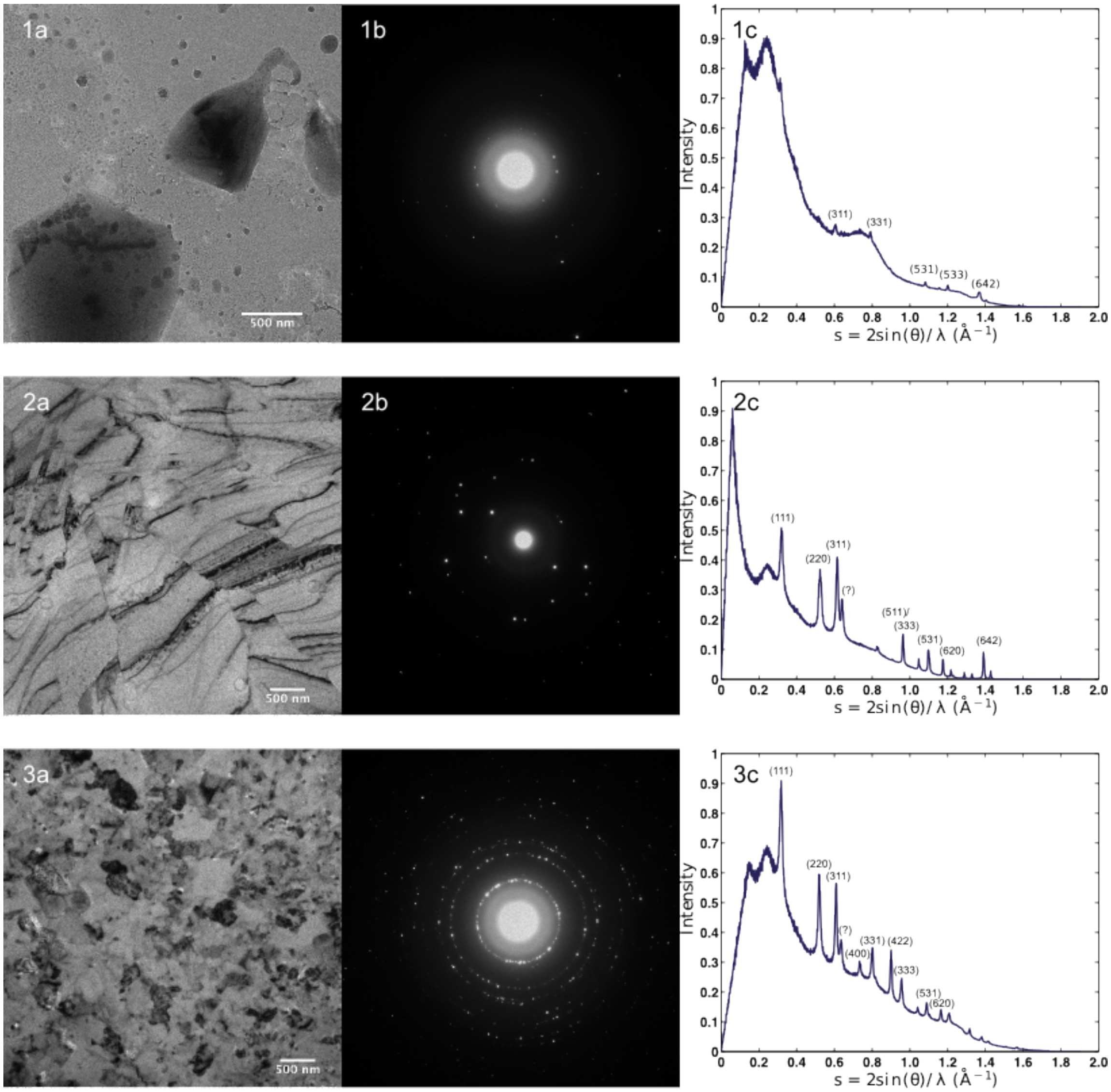

Figure 3–6: (a)TEM images, (b) diffraction patterns and (c) plot of intensity (arbitrary units) versus s for the three regions of interest.

3.3 Heat Diffusion and Estimate of Film Temperature

As a check on the interpretation of the results presented in Section 3.1, the time-evolution of the temperature distribution in the silicon thin film was calculated. The surface of the sample was illuminated by a pump laser with a 100 μm diameter spot size. This is a very large diameter compared to the film thickness (130 nm). Due to the large heat gradient in the direction of the film thickness, the heat conduction in the plane is much slower than the conduction through in the z-direcion. Thus, only the conduction through the thickness of the film needs to be considered.

3.3.1 Analytical Solution

As described in Section 1.2.3, the temperature distribution in a thin film can be calculated by solving the heat diffusion equation. The temperature distribution immediately after the pump pulse is given by Eq. 1.10. Assuming the film is perfectly insulated such that there is no heat flow out of the film and assuming that the thermal properties of the film remain constant, the solution to the 1D heat equation in the z-direction is

$$u(z,t) = \frac{1}{2}c_0 + \sum_{n=1}^{\infty} c_n \cos\left(\frac{n\pi z}{L}\right) e^{-\frac{k}{C_p\rho}\left(\frac{n\pi}{L}\right)^2 t} \tag{3.1}$$

where $u(z,t)$ is the 1D temperature distribution in the film and c_n are constants given by

$$c_n = \frac{2}{L}\int_0^L \cos\left(\frac{n\pi z}{L}\right) u(z,0)dz. \tag{3.2}$$

which are determined using the initial temperature distribution in the film, $u(z,0)$, resulting from the assumed impulsive laser excitation.

Using the optical and thermal properties for amorphous silicon found in 3–1, and a pulse energy of 180 mJ cm^{-2}, which corresponds to the average fluence for the illuminated area in Fig. 3–5, the temperature profile was determined for various

TABLE 3–1: Optical and thermal constant of amorphous, crystalline and liquid silicon, and the SiO_2 substrate. [36] [26]

	R at 532 nm	α at 532 nm (cm^{-1})	T_m (K)	ρC_p ($J\,\mathrm{cm}^{-3}\,\mathrm{K}^{-1}$)	k ($W\,\mathrm{cm}^{-1}\,\mathrm{K}^{-1}$)	ΔH ($J\,\mathrm{cm}^{-1}$)
a-Si	0.48	1×10^5	1418 ± 40	2.5	0.013	2900 ± 160
c-Si	0.36	2×10^4	1687	2.3	0.23	4158
l-Si	0.72	1×10^7	-	3.1	0.5	-
SiO_2	0.04	1	1893	2.6	0.007	-

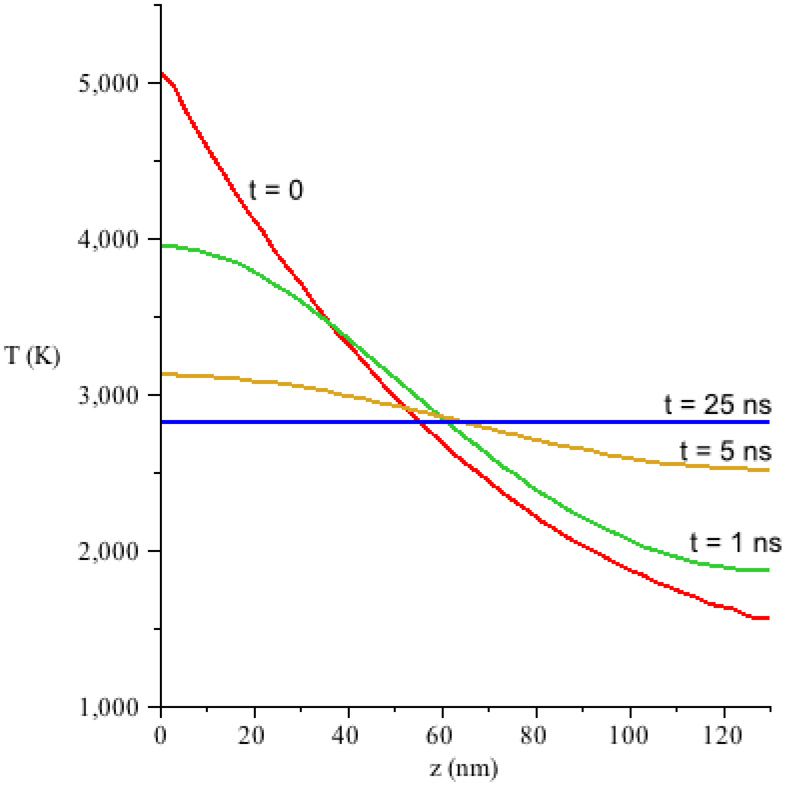

FIGURE 3–7: Film temperature as a function of depth for an incident fluence of $180\,\mathrm{mJ\,cm^{-2}}$.

times after excitation. These profiles are plotted in Fig. 3–7. $t = 0$ corresponds to the temperature distribution immediately after the arrival of the laser pulse.

The film temperature after 25 ns was 2820 K. The analytical solution assumes, however, that the thermal properties of the material do not change, which is obviously not the case since this temperature is well above the melting temperature of amorphous silicon.

From Fig. 3–7, it is clear that the film melts extremely quickly, on the order of the pump pulse duration and that this simple model of the heat conduction is insufficient . It is thus important to include the phase change in the model, along with the associated changes in thermal and optical properties of the silicon that occur as a result. It is also important to consider the non-impulsive nature of the laser excitation.

3.3.2 Heat Diffusion Model Including Melting

As the laser pulse heats the sample beyond the melting point, the optical and thermal properties are changed drastically. In order to correctly handle the transition from solid amorphous silicon to liquid silicon, the heat diffusion equation must be solved numerically including the correct temperature dependence of the material properties.

In order to model the temperature evolution in the z-direction in the silicon film, I have followed the approach outlined in chapter 4 of Laser Annealing of Semiconductors [36]. The complete MATLAB code can be found in Chapter A.

In this method, the sample is divided into ‘i’ slices of thickness Δz. Time zero is taken as the start of the laser pulse. For each time ‘t’ and slice ‘i’, the temperature, T_{b_i}, the structure (amorphous, liquid or crystalline) and, if the melting temperature is reached, the fraction of the layer which has melted is computed.

At the surface of the film, the incident laser power is

$$I_1 = I_0(t)(1 - R) \tag{3.3}$$

where $I_0(t)$ is gaussian in the time dimension. For the laser used in these experiments with a FWHM of 15 ns.

The power reaching the ith layer is

$$I_i = I_{i-1} e^{-\alpha_{i-1}\Delta z}. \tag{3.4}$$

To calculate the new temperature, T_{a_i} at time $t + \Delta t$, first the energy absorbed from the laser pulse during this time interval is calculated: The energy absorbed in time Δt is

$$\Delta Q_{abs} = I_i(1 - e^{-\alpha_i \Delta z})\Delta t. \tag{3.5}$$

The energy per unit area transfered to the nearest-neighbour layers is

$$\Delta Q_{diff} = \left(\kappa_- \frac{T_{b_{i-1}} - T_{b_i}}{\Delta z} + \kappa_+ \frac{T_{b_{i+1}} - T_{b_i}}{\Delta z}\right) \Delta t \tag{3.6}$$

where

$$\kappa_- = (\kappa_{i-1} + \kappa_i)/2 \qquad \text{and} \qquad \kappa_- = (\kappa_{i-1} + \kappa_i)/2 \tag{3.7}$$

The new temperature after heat absorption and diffusion is calculated from

$$T_{a_i} = T_{b_i} + \frac{\Delta Q_{abs} + \Delta Q_{diff}}{C_p \rho \Delta z}. \tag{3.8}$$

If the film is melting or solidifying, the latent heat of the transition must be included in the computation and Eq. 3.8 cannot be used. Instead, the energy available for melting (or released from the solidification), given by

$$\Delta Q' = \Delta Q_{abs} + \Delta Q_{diff} - (T_m - T_{b_i})C_p \rho \Delta z \tag{3.9}$$

is calculated. With this numerical approach, it is possible for more than one state to exist in a single layer, in which case, we must keep track of the fraction of each layer that has melted

$$\Delta FF = \frac{\Delta Q'}{\Delta H_m \rho \Delta z} \tag{3.10}$$

This increment is added to the existing melted fraction, $FF_i(t)$, and $FF_i(t + \Delta t$ is used to calculate $\Delta Q''$, the heat available for raising (or lowering, if negative) the temperature following melting (or solidification).

The new temperature of the film is then calculated as follows:

$$T_{a_i} = T_m + \frac{\Delta Q''}{C_p \rho \Delta z}. \tag{3.11}$$

To avoid instabilities in the modeling, it is crucial that certain stability criteria is met. The time increment is related to the slice thickness by the stability relation:

$$\frac{\kappa \Delta t}{C_p \rho}(\Delta z)^2 < \frac{1}{2}. \tag{3.12}$$

The initial temperature ($t = 0$) is set to $T = 300\,\mathrm{K}$ throughout the film and substrate. The boundary condition at the top surface of the film assumes no loss of heat from the illuminated surface. This is a fairly good assumption since the sample was under vacuum, so there is heat exchange minimal heat exchange with the surroundings. Heat loss through blackbody radiation could be included in the model, but it is likely negligible on the time scale investigated.

The boundary condition at the substrate is slightly more complicated. Although SiO_2 does not absorb the 532 nm pump pulse due to the low reflectivity and long absorption length at this wavelength, it can conduct heat from the sample. Thus it is not valid to assume the substrate is insulating. Since the substrate is very thin, it is also a poor assumption to model the oxide as a heat sink at a constant temperature.

Thus, the substrate is allowed to act as a heat bath; heat can be conducted to or from the substrate, but the substrate temperature is not allowed to vary independently of the film temperature.

The the thermal conductivity of the substrate is approximately half that of a-Si, but the heat capacity is similar. An improved conduction model would treat the substrate a series of slices in thickness with different optical and thermal properties than the silicon and model the temperature in both the sample and substrate using the same algorithm. Because this model is very computationally intensive, the simplified model which allowed conduction of heat *to* the substrate but did not calculate conduction *within* the substrate was chosen.

Since this model is in one dimension only, heat diffusion in the radial direction from the centre of the pump pulse is neglected. The lateral heat diffusion was modeled independently of the diffusion in the z-direction and,due to the gradual temperature gradient in this direction, was found to be very slow (on the order of milliseconds) and thus can be neglected on short time scales.

Fig. 3–8 shows the model's results for the same incident fluence used to in the analytical results, shown in Fig. 3–7. Time zero in this figure is the *beginning* of the pump pulse, which has a duration of 15 ns at FWHM. The maximum temperature in the film is reached within the first 20 ns after the beginning of the pulse, which corresponds to the peak of the illumination. This temperature is much lower than was calculated analytically, as the computational model shows only the first few nanometers of the film reach the melting temperature. At 47 ns, energy is no longer being absorbed from the pump pulse and the temperature begins to drop off very rapidly as the surface layer is crystallized.

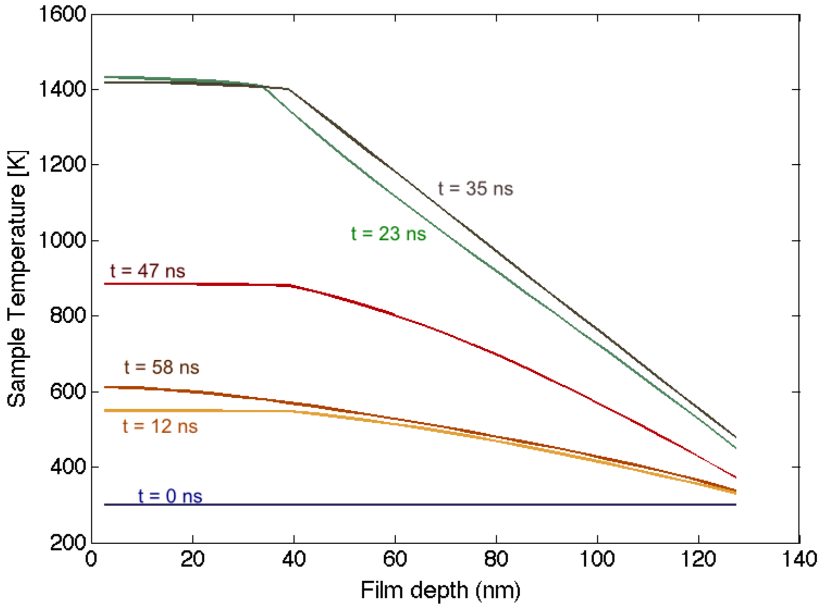

FIGURE 3–8: Results of the heat conduction modeling for an incident fluence of 180 mJ cm^{-2}.

Melt Boundaries

The pump pulse is gaussian in the transverse dimension and arrives at the sample at a 45° angle, illuminating an elliptical area. By fitting ellipses to the boundary between dewetted region and the large crystalline region (boundary 'a') and the boundary between the large and small crystal regions (boundary ' b'), as shown in Fig. 3–9, the limit for complete and partial melting of the silicon film can be estimated. This process was repeated on several images taken at different pulse energies.

Based on these measured boundaries, the fluence required to melt a surface layer of the silicon film is 240 ± 20 mJ cm^{-2}. The threshold for complete melting of the 130 nm film is approximately 330 ± 20 mJ cm^{-2}. The results of the heat diffusion model at these fluences are shown in Fig. 3–10.

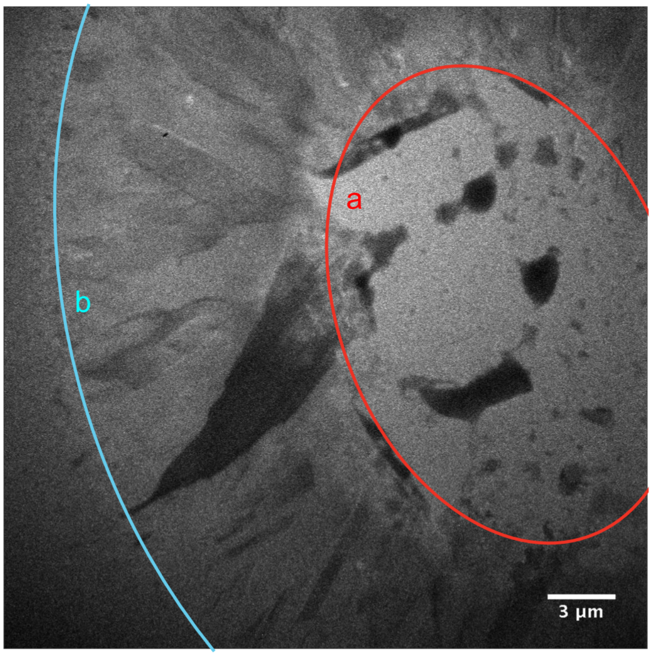

FIGURE 3–9: At boundary a sufficient energy is absorbed to melt the entire film. Between boundaries a and b, the film is only partially melted and outside boundary b, the film does not absorb enough energy to melt.

At the dewetting boundary, the imaging suggests that entire film is melted. The model results at a fluence of 330 mJ cm^{-1} (Fig. 3–10.a) leave the silicon/substrate interface unmelted. About 30 ns after the start of the pump pulse, the film begins to cool. After an additional 15 ns, the silicon has cooled sufficiently to resolidify. To completely melt the film within the model, the fluence required is 330 mJ cm^{-1}. This value is only 8% higher than the experimental fluence.

In Fig. 3–10.b, the top surface of the thin film is melted but the silicon near the substrate never liquifies. The incident fluence used to calculate this temperature profile was 240 ± 20 mJ cm^{-2}. According to the results of the heat conduction model, the minmum fluence for surface melting is 195 mJ cm^{-2}. This is 19% smaller than the image fluence. It is possible that it is necessary to melt not just the surface

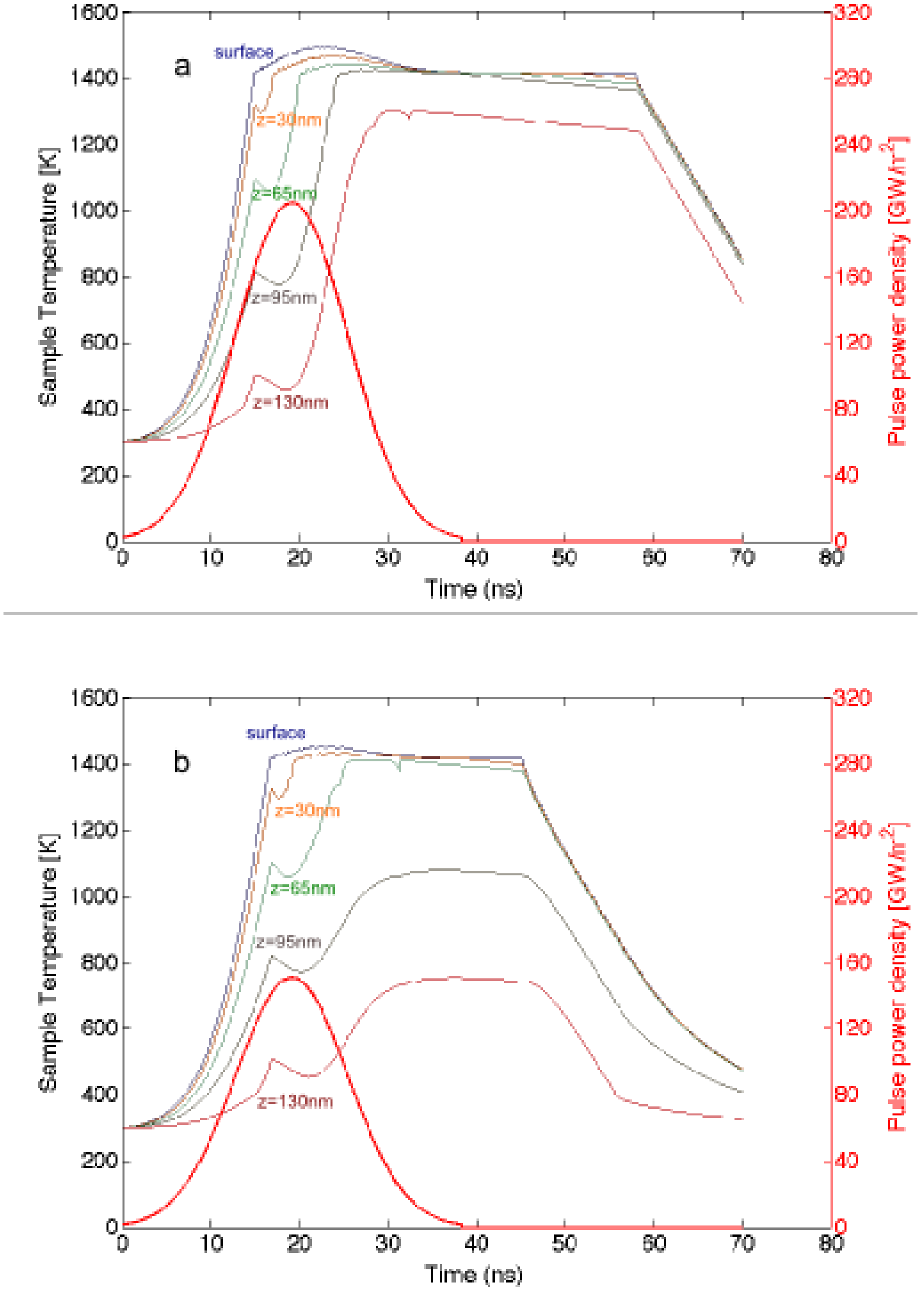

Figure 3–10: Heat diffusion modelling showing the temperature profile as a function of time at various depths in the silicon film. The temperature is plotted for the experimentally determined fluences (a) at the dewetting boundary ($330 \pm 20\,\mathrm{mJ\,cm^{-2}}$) and (b) is at the surface melting boundary ($240 \pm 20\,\mathrm{mJ\,cm^{-2}}$).

layer, but some minimum film thickness in order to achieve the large grained crystal structures observed in Section 3.1.

The percent differences between the modeled and experimental fluences were 8% and 19% for the dewetting boundary and the surface melt boundary respectively. More accurate modeling of the heat conduction to the SiO_2 substrate may improve the agreement between this model and observations.

3.4 Inconsistencies in Experimental Results

Although it was generally observed that the diameter of the crystallized or melted region grew with increasing fluence, minor divergences from this trend were observed on a single sample grid. This discrepancy is most likely due to the pulse's proximity to the edge of the window, however, I was unable to confirm this theory since the sample was too badly damaged to perform a complete study in the TEM at McGill.

There also seems to be a large variation in the results from one sample to another. The range of fluences used on the sample discussed in Section 3.1 were generally much higher than those that produced similar results on a second sample. Also, the film did not delaminate from this sample discussed as it had in a prior experiment (see Fig. 3–11. It is unclear, presently, what is behind these variations, but some possibilities to be investigated include variations in the thickness of the silicon film, uniformity of the substrate, or changes to the pump laser from one day to another (ie. a larger or smaller spot size at the sample).

All the SiO_2 windows used in this experiment were produced from the same wafer, and the oxide thickness was fairly uniform. Over the 100 mm wafer, the oxide thickness varied by only 5% . Similarly, the deposition of the a-Si was done on all of the samples at the same time. There are always small variations due to

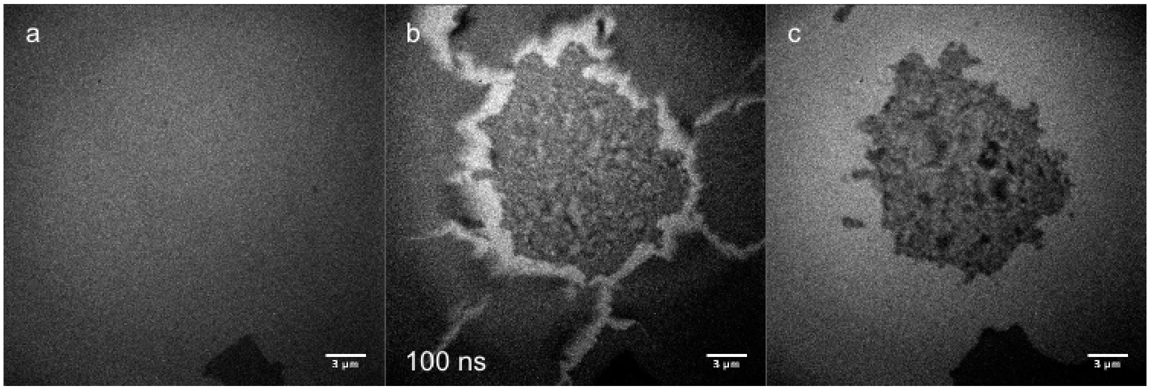

FIGURE 3–11: Time series for 135 mJ cm^{-2} laser pulse. (a) before exposure, $t = 0$ (b) $t = 100$ ns after the pump pulse, (c) $t = \infty$. There is a small crystallized area at the centre of the pulse, but the remainder of the silicon film has delaminated from the substrate.

the position in the chamber, but this also would likely be only a few nanometers difference in thickness. If these small variations in the sample are, in fact, the source of the observed variations between sample grids, the sample preparation procedure may require revision. Further experiments are needed to determine the root of these inconsistencies in the crystallization results.

3.5 Germanium Crystallization

A natural extension to the investigation of the crystallization of a-Si is to repeat the experiments with a different, but similar material. Another well-used semiconducting material is germanium. Silicon and germanium have similar optical and thermal properties, and both make fcc crystal latices, making them good candidates for a comparative study. A knowledge of the dynamics of crystallization in a-Ge will complement what has already been learned in the silicon studies.

Amorphous Ge has a similar reflectivity to a-Si but the absorption length is approximately half that of silicon, meaning that the pump laser energy will be more heavily deposited near the surface of the film. The melting temperature of germanium is also much lower than that of silicon. These optical and thermal properties are summarized in 3–2.

TABLE 3–2: Optical and thermal constant of a-Ge and c-Ge. [36]

	R at 532 nm	α at 532 nm ($/unitcm^{-1}$)	T_m (K)	ρC_p ($J\,\mathrm{cm}^{-3}\,\mathrm{K}^{-1}$)	ΔH ($J\,\mathrm{cm}^{-3}$)
a-Ge	0.47	2×10^5	850	1.76	1597
c-Ge	0.49	6.7×10^4	1232	1.76	2188

3.5.1 Time-Resolved Results on a-Ge on SiO_2

DTEM images were obtained for a-Ge on SiO_2 substrates. The images in Fig. 3–12 were obtained for an average fluence of 115 mJ cm^{-2} illuminated the sample. This is comparable to the lowest fluence investigated in silicon. Similar to the silicon samples, the film completely melted and dewetted at the centre of the pump pulse, but notably absent in the germanium samples are the large radially-oriented grain structures which were observed in silicon. In fact, from Fig. 3–12.1c, which captures the periphery of the melted region, there is very little resolvable structure. It is probable that there is some crystalline material present, but that the grains are too small or the contrast is too poor to resolve with the DTEM.

The germanium film is melted extremely quickly. As seen in Fig. 3–12.3b and c, there are only very small changes between the $t = 100$ ns image and the final image. In fact, at 70 ns much of the final structure is already visible in Fig. 3–12.2b.

The film seems to dewet from the substrate much more easily than for a-Si. This is likely dominated by the melting temperature and the latent heat of fusion of a-Ge, which are much lower than for a-Si, but the substrate may also play a role. A different substrate material to which the germanium adheres more readily is needed to profitably study crystallization in a-Ge.

When the ‘droplets’ of dewetted germanium were examined using a conventional TEM, they were found to be too thick for either electron diffraction or dark field imaging, so the precise nature of these droplets is unknown. Based on the experiments on silicon, however, it is likely that they are crystalline.

3.5.2 ‘Cell’-like Structures Observed in a-Ge on SiN

Experiments on an a-Ge film on 100 nm thick SiN windows have yielded some strange results. For a single pump pulse, multiple randomly distributed, apparently isolated spots appeared on the sample. These structures are shown in Fig. 3–13. The emergent structures were roughly circular and cell-like in appearance, each with a dark ‘nucleus’ surrounded by a region of lighter contrast. The average fluence on the sample was approximately 90 mJ.

At first it was postulated that these spots were the result of diffraction of the pump beam, so that multiple laser pulses were exciting the sample rather then having one large area of illumination. To check whether this was the case, we switched to a titanium film, which would typically be used to align the pump beam with the electron pulse. On the titanium foil, there was clearly only one laser spot, which convincingly ruled out beam diffraction as the source of the cell structure on the a-Ge sample. In addition, the cells were randomly located within the exposed area. If they were the result of a diffracted pump beam, their relative position would be orderly.

The *ex situ* TEM images, in Fig. 3–13.b-d, show that the cell structures are composed of extremely fine grained p-Ge. The ‘nuclei’ measure approximately 1 μm in diameter, with the total cell diameter ranging from $2 - 5\,\mu$m.

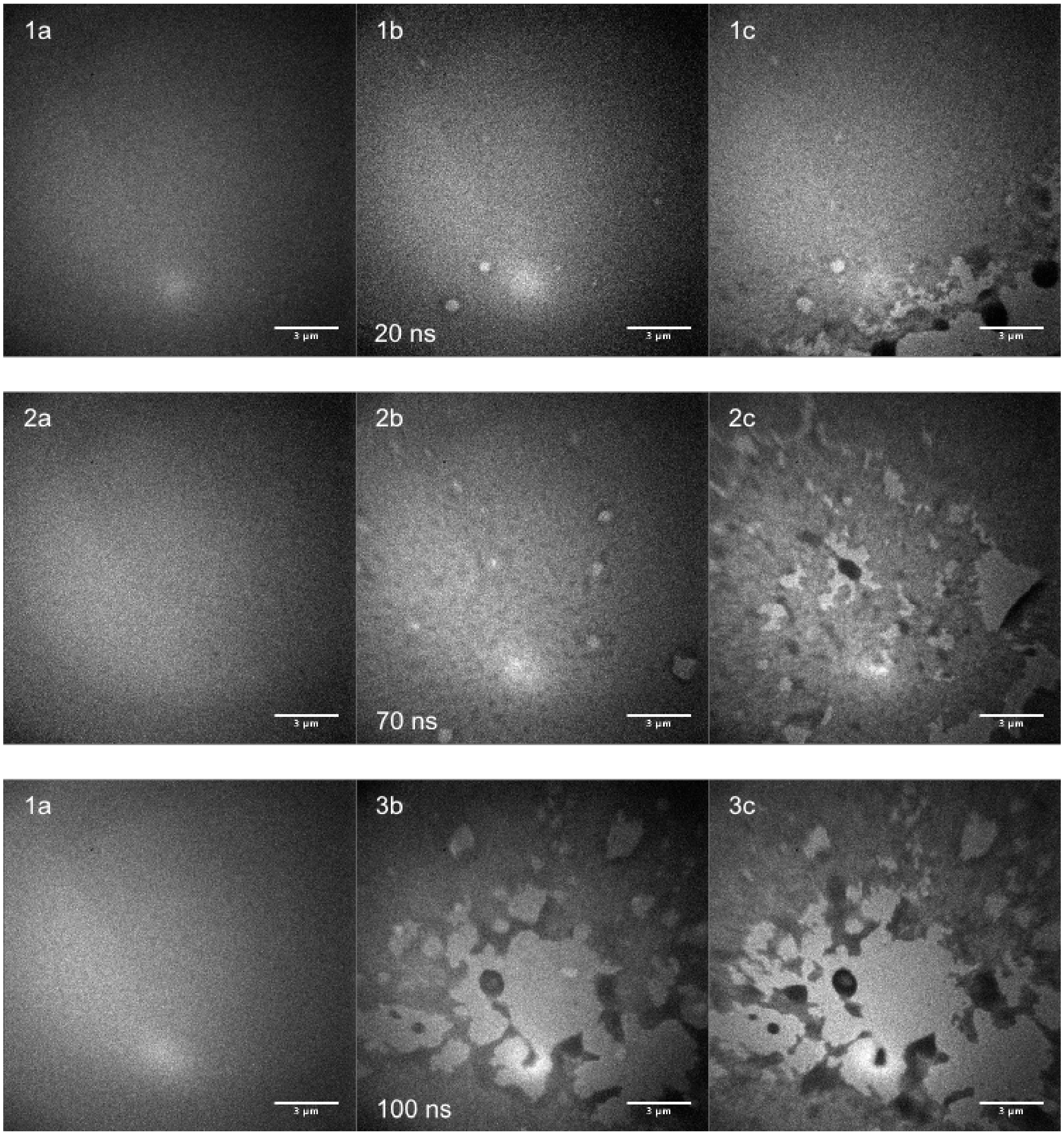

Figure 3–12: Time series for $115\,\mathrm{mJ\,cm^{-2}}$ laser pulse. (a) before exposure, $t = 0$ (1b) $t = 20\,\mathrm{ns}$ after the pump pulse, (2b) $t = 70\,\mathrm{ns}$, (3b) $t = 100\,\mathrm{ns}$, (c) $t = \infty$. The pump laser was not well aligned in the first set of images, so only the edge of the melted area is visible. The scale bar in each frame is $3\,\mu\mathrm{m}$.

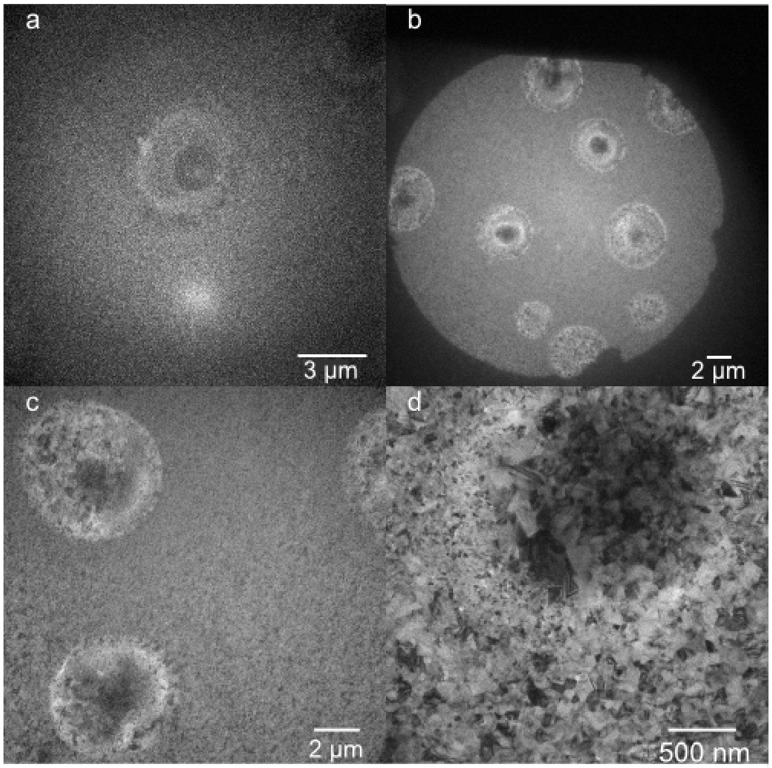

Figure 3–13: Anomalous disk structures resulting from a single pump pulse in the DTEM. (a) pulsed image taken at $t = \infty$ in the DTEM (b - d) TEM images taken *ex situ* at various magnifications. The darkened area in (b) is due to the objective aperture in the microscope.

In the DTEM, each window on this sample was irradiated in turn and each time resulted in a random distribution of cell structures over the illuminated area. Unfortunately, no time-resolved images were taken. Despite the consistency throughout this sample, these strange results have yet to be reproduced on another a-Ge sample, on SiN or otherwise.

It is possible that nucleation of these cells in the film is random, or else there are preferred sites present in the amorphous film where due to local stresses or impurities, there is a lower threshold energy for crystallization. No such imperfections were visible in the images or diffraction patterns on the a-Ge films, which, before the pump pulse, appeared to be uniformly amorphous. These structures are, however, quite intriguing, and it may be interesting to investigate this further. Perhaps time-resolved images of this process would elucidate mechanism which produces these strange results.

CHAPTER 4

Conclusion

4.1 Summary of Results

The laser-induced crystallization of thin film amorphous semiconductors was studied *in situ* in the DTEM at LLNL. Both a-Si and a-Ge deposited by e-beam evaporation onto SiO_2 windows were investigated, through time-resolved, real space imaging.

On the a-Si sample, three distinct regions were observed. At the centre of the gaussian pump pulse, the entire silicon film was melted. The silicon in this region dewetted from the substrate and coalesced into crystalline or polycrystalline droplets of various size on the substrate surface. Farther from the peak of the pulse, the energy absorbed by the silicon was not sufficient to melt the entire film. The a-Si near the substrate remained solid, so the silicon did not dewet. Instead, in this near complete melting region, the top layers of the film recrystallized as large, radially oriented crystal grains. Outside the melting region, where the temperature of the film does not exceed the melting temperature, the film undergoes solid-state crystallization, resulting in a polycrystalline film with crystals on the order of tens to hundreds of nanometers in diameter.

A simple thermodynamic model of the pulsed laser heating of the silicon was used to calculate the temperature in the film by modelling the heat conduction in one dimension. This model supported my interpretation of the results obtain in the DTEM experiment.

Preliminary experiments were made on a-Ge, but more data is needed to characterize how the crystallization in germanium depends on the incident fluence.

4.2 Future Work

The DTEM at LLNL was uninstalled in May of 2009 to be moved to a new laboratory space. Moving a complicated instrument such as this is not trivial and at the time of writing, the microscope is still not operational. As a result, I was unable to perform any follow-up experiments on either a-Si or a-Ge. Thus, there are several experiments planned which may clarify the source of some of the discrepancies described in Section 3.4, as well as exploring the solid-state crystallization in a-Si and extending the study of a-Ge crystallization.

Several new features are planned to be implemented to the DTEM, which will allow certain experiments to be performed that were very difficult or not possible in the current instrument. In particular, there is a plan to add 'movie mode' capabilities to the DTEM. Movie mode allows multiple timed images to be captured in a single experiment, which makes it possible to track the nucleation and growth of a single crystal, or the development of defects in a sample with time.

4.2.1 Silicon

The results obtained so far on a-Si have laid the ground work for a more comprehensive study of semiconductor crystallization. More data is required to determine the rate at which the nucleation and growth occurs and to explore the source of discrepancies between different samples which were produced under identical conditions.

Thus far, this study has focused mainly on the melt-mediated crystallization of the film, meaning the silicon was liquified before it crystallized. An investigation at lower pulse energies would allow the solid state crystallization of a-Si to be explored.

Better contrast and higher spatial resolution is needed to study defect formation in the crystallized silicon. Defects and grain boundaries have a large impact on the electron mobility in thin film transistors, so an understanding of these dynamics would likely have a significant impact on the advancement of this technology. Unfortunately, such an experiment is not achievable with the current state of the art DTEM. Long-term plans for improvements to the optics and electron source may make such an experiment possible.

4.2.2 Germanium

The preliminary experiments performed on a-Ge have had mixed results. The study should be expanded to a wider range of pulse energies. Applying the heat conduction model which was used to model the temperature profile in a-Si may be helpful in selecting an appropriate range of fluences to investigate.

The strange, cell-like structures observed in the a-Ge deposited on SiN warrants further investigation. In particular, no time resolved experiments were made on this sample. Only the structures before and long after the pump pulse were obtained. Time resolved images are needed to determine the dynamics which have led to these results.

4.3 Outlook

Studying the crystallization dynamics of amorphous silicon *in situ* through real space imaging and diffraction patterns will lead to a better understanding of the transient states, which will in turn provide insight into the crystallization process in general.

The ability to precisely control the structural properties of semiconductors is vitally important in industry, for the production and development of a vast range of technologies. An understanding of the dynamics leading to these microstructures may lead to superior control over the output structure and thus more optimal device properties. Specifically, a knowledge of the crystallization dynamics of thin film a-Si on SiO_2 would likely have technological significant implication in the design and processing of thin film transistors.

As improvements are made to the resolution, DTEM has the potential to shed light on many important scientific phenomena which occur on short time scales, from the kinetic pathways of chemical reactions to the function of biological processes.

APPENDIX A

Heat Diffusion Modeling

A.1 heatflow.m

This function models the heat diffusion in a film by calculating the temperature distribution in slices of the film for increments in time.

```matlab
function [M,t_vec,z_vec,I] = heatflow(z,N_z_slices,t,N_t_slices,pulse_energy,pulse_width_t,T_i,state_i,FF_i,Tm,Hm,abs_params,Cp,kappa,R,substrate_condition,T_subs,kappa_subs,Δ_T_subs)

    % z - total film thickness
    % N_z_slices - number of slices in z
    %
    % t - total time to evaluate
    % N_t_slices - number of slices in t
    %
    % pulse_energy - total pulse energy over space and time
    % pulse_width_t - equivalent to sigma for the pulse width in time
    %
    % T_i - initial temperature (K)
    % state_i - initial state (1 for crystalline, 2 for amorphous, 3 for liquid)
    % FF_i - initial fill factor (fraction of the material that has been melted - should be 0)
    % Tm - melting temperature of the amorphous phase (K)
    % Hm - enthalpy of melting per unit mass (J/g)
    %
    % THE FOLLOWING PARAMETERS ARE SET AS 3-CELLS REPRESENTING THE VALUES FOR:
    % {CRYSTALLINE, AMORPHOUS, LIQUID}
    % abs_params - 1/absorption length (1/m)
    % Cp - specific heat at constant pressure (J/g K)
```

```
% kappa - thermal conductivity (W/m K)
% R - reflectivity.  All entries take 2-vectors of the form [b,↘
→m] where R=mT+b.  An entry of only one number will assume m=0 ↘
→(ie: constant over temperature)
% substrate_condition - 0 for fully insulating substrate, 1 for↘
→ perfect heat sink, 2 for a heat sink that is either at T_subs↘
→ or a fixed temperature below the temperature of the last ↘
→layer (defined by ∆_T_subs)
% T_subs - initial temperature of the substrate
% kappa_subs - thermal conductivity of the substrate
% ∆_T_subs - fixed difference between substrate and the last ↘
→layer

if nargin<16, substrate_condition = 0; end
if nargin<17, T_subs = T_i; end
if nargin<18, kappa_subs = 0.007*100; end
if nargin<19, ∆_T_subs = 100; end

FLOATING_POINT_SAFETY_FACTOR = 2;

dz = z/N_z_slices;  z_vec = (dz/2):dz:z;
dt = t/N_t_slices;  t_vec = (dt/2):dt:t;

% Check stability condition for input
for i = 1:3
    if dt ≥ Cp{i} * dz^2 / (2*kappa{i})
        fprintf('ERROR, stability condition not satisfied!\n');
        fprintf('[i, Cp{i}, kappa{i}, dt, dz]\n');
        M = [i, Cp{i}, kappa{i}, dt, dz]
        fprintf('dt must be less than:');
        dt = Cp{i} * dz^2 / (2*kappa{i})
        N_t_slices = t/dt
        return
    end
end

% Setup master time/z-slices matrix with initial conditions
M = {};
in_conditions = [T_i, state_i, FF_i];
dti = 1;
for dzi = 1:N_z_slices
    M(dti,dzi) = {in_conditions};
end

for dti = 1:N_t_slices-1
    if mod(dti,1000) == 0
        dti % Print the layer that is computing so that we can ↘
        →see progress
    end
    % Find reflectivity of first z-layer at this time
```

```
        R_0 = reflectivity(M(dti,1), R);

        % Find incident power for each cell in z as a single matrix
        % First layer power is:
        if t_vec(dti) > 6*pulse_width_t,
            I = 0; %cut off the power after 6 sigma to prevent non-↘
            →physical modelling of perpetual addition of small ↘
            →amounts of energy
        else
            I = pulse_energy/(sqrt(2*pi)*pulse_width_t) * exp(-(↘
            →t_vec(dti) - 3*pulse_width_t)^2/(2*pulse_width_t^2))* ↘
            →(1 - R_0);
        end

        % Incident power reaching subsequent layers are found layer↘
        →-by-layer
        for dzi = 2:N_z_slices
            I(dzi) = I(dzi-1)*exp(-getparam(M(dti,dzi-1),abs_params↘
            →) * dz);
        end

        for dzi = 1:N_z_slices
            % Eq A3
            dQ_abs = I(dzi)*(1-exp(-getparam(M(dti,dzi),abs_params)↘
            → * dz)) * dt;

            % Eqs A4 and A5 built up part by part, with options for↘
            → dealing with the substrate conditions
            this_kappa = getparam(M(dti,dzi),kappa);
            this_T = M{dti,dzi}(1);
            this_state = M{dti,dzi}(2);
            this_FF = M{dti,dzi}(3);

            dQ_vert = 0;
            if dzi > 1
                k_up = mean([getparam(M(dti,dzi-1),kappa), ↘
                →this_kappa]);
                T_up = M{dti,dzi-1}(1);
                ∆_T = abs(T_up - this_T);
                if (∆_T > FLOATING_POINT_SAFETY_FACTOR*eps(T_up)) ↘
                →&& (∆_T > FLOATING_POINT_SAFETY_FACTOR*eps(this_T)↘
                →) %insurance that we will not see floating point ↘
                →errors
                    dQ_vert = dQ_vert + k_up * (T_up - this_T)/dz;
                end
            end
            if dzi < N_z_slices
                k_down = mean([getparam(M(dti,dzi+1),kappa), ↘
                →this_kappa]);
                T_down = M{dti,dzi+1}(1);
```

```
            Δ_T = abs(T_down - this_T);
            if (Δ_T > FLOATING_POINT_SAFETY_FACTOR*eps(T_down))↘
            → && (Δ_T > FLOATING_POINT_SAFETY_FACTOR*eps(this_T↘
            →))
                dQ_vert = dQ_vert + k_down * (T_down - this_T)/↘
                →dz;
            end
        end

        % Account for options dealing with substrate conditions↘
        → (1 or 2)
        % Substrate acts as a perfect heat sink
        if (dzi == N_z_slices) && (substrate_condition == 1)
            k_down = kappa_subs;
            T_down = T_subs;
            Δ_T = abs(T_down - this_T);
            if (Δ_T > FLOATING_POINT_SAFETY_FACTOR*eps(T_down))↘
            → && (Δ_T > FLOATING_POINT_SAFETY_FACTOR*eps(this_T↘
            →))
                dQ_vert = dQ_vert + k_down * (T_down - this_T)/↘
                →dz;
            end
        end
        % Substrate acts as a heat sink that is kept a constant↘
        → difference below the lowest layer's temperature, ↘
        →without going below the set substrate temperature.
        if (dzi == N_z_slices) && (substrate_condition == 2)
            k_down = kappa_subs;
            T_down = max([this_T - Δ_T_subs, T_subs]);
            Δ_T = abs(T_down - this_T);
            if (Δ_T > FLOATING_POINT_SAFETY_FACTOR*eps(T_down))↘
            → && (Δ_T > FLOATING_POINT_SAFETY_FACTOR*eps(this_T↘
            →))
                dQ_vert = dQ_vert + k_down * (T_down - this_T)/↘
                →dz;
            end
        end

        % Final form of A4 (corrected to remove absolute value ↘
        →thus
        % allowing cooling as well as heating from neighbours)
        dQ_diff = dQ_vert * dt;

        % Eq A6
        T_ai = this_T + (dQ_abs + dQ_diff)/(getparam(M(dti,dzi)↘
        →,Cp) * dz);

        if (this_T == Tm) || ((this_T < Tm) && (Tm ≤ T_ai)) || ↘
        →((T_ai ≤ Tm) && (Tm < this_T))
            % Melting or solidification processes have occurred
```

```

                % Eq A7
                ∆_T = abs(Tm - this_T);
                if (∆_T > FLOATING_POINT_SAFETY_FACTOR*eps(Tm)) && ↘
                →(∆_T > FLOATING_POINT_SAFETY_FACTOR*eps(this_T))
                    dQprime = dQ_abs + dQ_diff - (Tm - this_T)*↘
                    →getparam(M(dti,dzi),Cp)*dz;
                else
                    dQprime = dQ_abs + dQ_diff;
                end

                % Eq A8
                dFF = dQprime/(Hm * (dz));

                % Calculate new FF for this cell
                newFF = this_FF + dFF;

                if (0 ≤ newFF) && (newFF ≤ 1)
                    newT = Tm;
                    newState = this_state;
                else
                    if newFF > 1
                        dQprimeprime = (newFF - 1) * (dz) * Hm;
                        newFF = 1;
                        newState = 3;
                    else
                        %newFF < 1
                        dQprimeprime = newFF * (dz) * Hm;
                        newFF = 0;
                        newState = 1;
                    end

                    newT = Tm + dQprimeprime/(getparam(M(dti,dzi),↘
                    →Cp) * dz);
                end
            else
                % No melting or solidification processes occurred.
                newT = T_ai;
                newState = this_state;
                newFF = this_FF;
            end

            % Set this cell's values for the next time step
            M(dti+1,dzi) = {[abs(newT), newState, newFF]};
        end
    end

    % Recalculate the incident pulse over time to output for ↘
    →illustration when plotting the results
```

```
    I = pulse_energy/(sqrt(2*pi)*pulse_width_t) * exp(-(t_vec - 3*↘
    →pulse_width_t).^2./(2*pulse_width_t^2));
    I(find(t_vec > 6*pulse_width_t)) = 0;

%↘
→--------------------------------------------------------------------↘
→
function R = reflectivity(T_state_FF, Refl_params)
    % Calculates the reflectivity based on the temperature, state, ↘
    →FF, and the appropriate
    % reflectivity parameters for the three states

    T = T_state_FF{1}(1);   state = T_state_FF{1}(2);   FF = ↘
    →T_state_FF{1}(3);
    FF = min([FF,1]);  FF = max([FF,0]);    % Force FF to be ↘
    →between 0 and 1

    % Extract the parameters into human-readable form (m is slope, ↘
    →b is intercept).
    % If scalar values provided, assume no slope (m=0)
    if length(Refl_params{1}) < 2, m_crystal = 0; else m_crystal = ↘
    →Refl_params{1}(2); end
    if length(Refl_params{2}) < 2, m_amorph = 0; else m_amorph = ↘
    →Refl_params{2}(2); end
    if length(Refl_params{3}) < 2, m_liquid = 0; else m_liquid = ↘
    →Refl_params{3}(2); end

    b_crystal = Refl_params{1}(1);
    b_amorph = Refl_params{2}(1);
    b_liquid = Refl_params{3}(1);

    % Calculate R as a combination of liquid and solid phases where↘
    → appropriate
    switch state
        case 1,
            R = (1 - FF) * (m_crystal*T + b_crystal) + FF * (↘
            →m_liquid*T + b_liquid);
        case 2,
            R = (1 - FF) * (m_amorph*T + b_amorph) + FF * (m_liquid↘
            →*T + b_liquid);
        case 3,
            R = m_liquid*T + b_liquid;
        otherwise,
            fprintf('heatflow:reflectivity - State is invalid.  ↘
            →Must be 1, 2, or 3');
    end
%↘
→--------------------------------------------------------------------↘
→

```

```
%↘
→──────────────────────────────────────────────────────────────────────────────────↘
→
function param = getparam(T_state_FF, separated_params)
    % Returns parameter based on the state and  FF,
    % and the parameters corresponding to the three states

    T = T_state_FF{1}(1);   state = T_state_FF{1}(2);   FF = ↘
    →T_state_FF{1}(3);  FF = min([FF,1]);
    FF = max([FF,0]);   % Force FF to be between 0 and 1

    param_crystal = separated_params{1};
    param_amorph = separated_params{2};
    param_liquid = separated_params{3};

    % Calculate alpha as a combination of liquid and solid phases ↘
    →where appropriate
    switch state
        case 1,
            param = (1 - FF) * param_crystal + FF * param_liquid;
        case 2,
            param = (1 - FF) * param_amorph + FF * param_liquid;
        case 3,
            param = param_liquid;
        otherwise,
            fprintf('heatflow:getparam - State is invalid.  Must be↘
            → 1, 2, or 3');
    end
```

A.2 runmodel.m

This function calls heatflow.m and inputs the thermal and optical properties and the initial and boundary conditions for the heat diffusion problem.

```
INVCM3TOINVM3 = (100)^(3); % conversion factor from 1/cm^3 to 1/m^3
INVCMTOINVM = 100; % conversion factor from 1/cm to 1/m

z = 130e-9; %film thickness (m)
N_z_slices = 25;
t = 70e-9; %time for simulation (s)
N_t_slices = 8.4e4;
pulse_energy = 2559; %J/m^2
pulse_width_t = 15e-9/(2*sqrt(2*log(2))); %standard deviation in ↘
→temporal axis (s)

%Initial state
T_i = 300; %(K)
state_i = 2; %amorphous
FF_i = 0;
```

```

Tm = 1418; %Melting temperature (K)
Hm = 2897*INVCM3TOINVM3; %Enthalpy of melting (J/m^3)

kappa_subs = 0.007*INVCMTOINVM;

rho = {2.32*INVCM3TOINVM3, 2.26*INVCM3TOINVM3, 2.2*INVCM3TOINVM3}; ↘
→%(g/m^3)
abs_params = {2e4*INVCMTOINVM,1e5*INVCMTOINVM,1e7*INVCMTOINVM}; %↘
→(1/m)
Cp = {2.3*INVCM3TOINVM3, 2.5*INVCM3TOINVM3, 3.1*INVCM3TOINVM3}; %(J↘
→/(m^3 K))
kappa = {0.23*INVCMTOINVM, 0.013*INVCMTOINVM, 0.5*INVCMTOINVM}; %(W↘
→/(K m))
R = {[0.36 0], [0.48 0], [0.72 0]};

%substrate_condition = 0;
T_subs = T_i;
kappa_subs = 0.007*INVCMTOINVM;
∆_T_subs = 100;

[M,t_vec,z_vec,I] = heatflow(z,N_z_slices,t,N_t_slices,pulse_energy↘
→,pulse_width_t,T_i,state_i,FF_i,Tm,Hm,abs_params,Cp,kappa,R,↘
→substrate_condition,T_subs,kappa_subs,∆_T_subs);
```

References

[1] O. Bostanjoglo and T. Rosin, Mikroskopie **32**, 190 (1976).

[2] A. Ischenko et al., Applied Physics B, Photophysics and Laser Chemistry **B32**, 161 (1983).

[3] J. Ewbank, L. Schafer, D. Paul, O. Benston, and J. Lennox, Review of Scientific Instruments **55**, 1598 (1984/10/).

[4] S. Williamson, G. Mourou, and J. Li, Physical Review Letters **52**, 2364 (1984/06/25).

[5] M. Dantus, S. Kim, J. Wuliamson, and A. Zewail, Journal of Physical Chemistry **98**, 2782 (1994).

[6] B. J. Siwick, J. R. Dwyer, R. E. Jordan, and R. J. D. Miller, Science **302**, 1382 (2003).

[7] H. Ihee et al., Science **291**, 458 (2001).

[8] T. Lagrange, G. H. Campbell, J. D. Colvin, B. Reed, and W. E. King, Journal of Materials Science **41**, 4440 (2006).

[9] W. E. King et al., Journal of Applied Physics **97**, 1 (2005).

[10] H. Rose, Science and Technology of Advanced Materials **9** (2008).

[11] L. Reimer and H. Kohl, *Transmission Electron Microscopy: Physics of Image Formation*, Number 36 in Springer Sereies in Optical Sciences, Springer, 5th edition, 2008.

[12] J. Cao et al., Applied Physics Letters **83**, 1044 (2003).

[13] J. Kim et al., Science **321**, 1472 (2008).

[14] K. Sokolowski-Tinten et al., Physical Review Letters **87**, 225701 (2001).

[15] A. Rousse et al., Nature **410**, 65 (2001).

[16] R. Chatelain, RF compression of electron bunches applied to ultrafast electron diffraction, Master's thesis, McGill University, 2008.

[17] J. Cao, H. Ihee, and A. Zewail, Chemical Physics letters **290**, 1 (1998).

[18] A. Zewail, Philosophical Transactions of the Royal Society A, Mathematics, Physics, Engineering, and Science **363**, 315 (2005).

[19] P. W. Hawkes and E. Kasper, *Principles of Electron Optics*, volume 3, Academic Press, 1996.

[20] G. Olson and J. Roth, Materials Science Reports **3** (1988).

[21] M. Thompson et al., Physical Review Letters **52**, 2360 (1984).

[22] H.-D. Geiler, E. Glaser, G. Gotz, and M. Wagner, Journal of Applied Physics **59**, 3091 (1986).

[23] W. Sinke, A. Polman, S. Roorda, and P. Stolk, Applied Surface Science **43**, 128 (1989).

[24] S.-J. Moon, M. Lee, and C. P. Grigoropoulos, Journal of Heat Transfer **124**, 253 (2002).

[25] J. Im, H. Kim, and M. Thompson, Applied Physics Letters **63**, 1969 (1993).

[26] S. Brotherton, Semiconductor Science and Technology **10**, 721 (1995).

[27] O. Bostanjoglo, Physica Status Solidi A Applied Research **70**, 473 (1982).

[28] O. Bostanjoglo, W. Marine, and P. Thomsen-Schmidt, Laser-induced nucleation of crystals in amorphous ge films, volume 54, pages 302 – 7, 1992.

[29] M. Grimaldi, P. Baeri, and M. Malvezzi, Physical Review B, Condensed Matter **44**, 1546 (1991).

[30] M. R. Armstrong et al., Ultramicroscopy **107**, 356 (2007).

[31] M. R. Armstrong, B. W. Reed, B. R. Torralva, and N. D. Browning, Applied Physics Letters **90** (2007).

[32] W. E. King, M. R. Armstrong, O. Bostanjoglo, and B. W. Reed, *Science of Microscopy*, chapter High speed electron microscopy, Springer, 2006.

[33] B. W. Reed et al., Microscopy and Microanalysis **15**, 272 (2009).

[34] K. Biswas and S. Kal, Microelectronics Journal **37**, 519 (2006).

[35] K. Sundaram, R. Sah, H. Baumann, K. Balachandran, and R. Todi, Microelectronics Engineering **70**, 109 (2003).

[36] J. Poate and J. W. Mayer, editors, *Laser Annealing of Semiconductors*, Academic Press, 1982.